J. Fluid Mech. (2012), *vol.* 700, *pp.* 148–186.
doi:10.1017/jfm.2012.108

Instability of secondary vortices generated by a vortex pair in ground effect

D. M. Harris† and C. H. K. Williamson

Sibley School of Mechanical and Aerospace Engineering, Upson Hall, Cornell University, Ithaca, NY 14853-7501, USA

(Received 17 August 2011; revised 2 February 2012; accepted 20 February 2012; first published online 18 April 2012)

In this work, we investigate the approach of a descending vortex pair to a horizontal ground plane. As in previous studies, the primary vortices exhibit a 'rebound', due to the separation of secondary opposite-sign vortices underneath each primary vortex. On each side of the flow, the weaker secondary vortex can become three-dimensionally unstable, as it advects around the stronger primary vortex. It has been suggested in several recent numerical simulations that elliptic instability is the origin of such waviness in the secondary vortices. In the present research, we employ a technique whereby the primary vortices are visualized separately from the secondary vortices; in fact, we are able to mark the secondary vortex separation, often leaving the primary vortices invisible. We find that the vortices are bent as a whole in a Crow-type 'displacement' mode, and, by keeping the primary vortices invisible, we are able to see both sides of the flow simultaneously, showing that the instability perturbations on the secondary vortices are antisymmetric. Triggered by previous research on four-vortex aircraft wake flows, we analyse one half of the flow as an unequal-strength counter-rotating pair, noting that it is essential to take into account the angular velocity of the weak vortex around the stronger primary vortex in the analysis. In contrast with previous results for the vortex–ground interaction, we find that the measured secondary vortex wavelength corresponds well with the displacement bending mode, similar to the Crow-type instability. We have analysed the elliptic instability modes, by employing the approximate dispersion relation of Le Dizés & Laporte (*J. Fluid Mech.*, vol. 471, 2002, p. 169) in our problem, finding that the experimental wavelength is distinctly longer than predicted for the higher-order elliptic modes. Finally, we observe that the secondary vortices deform into a distinct waviness along their lengths, and this places two rows of highly stretched vertical segments of the vortices in between the horizontal primary vortices. The two rows of alternating-sign vortices translate towards each other and ultimately merge into a single vortex row. A simple point vortex row model is able to predict trajectories of such vortex rows, and the net result of the model's 'orbital' or 'passing' modes is to bring like-sign vortices, from each secondary vortex row, close to each other, such that merging may ensue in the experiments.

Key words: vortex dynamics, vortex instability

† Present address: Department of Mathematics, Massachusetts Institute of Technology, 77 Massachusetts Avenue, Cambridge, MA 02139, USA. Email address for correspondence: dmh@math.mit.edu

1. Introduction

The study of vortex–ground interactions has practical applications, as well as relevance to turbulence. For instance, coherent vortices embedded in the boundary layer are critical ingredients in the self-sustaining nature of turbulent flow (see the reviews of Cantwell 1981; Robinson 1991; Panton 2001). Panton (2001) describes the process by which a vortex can roll up boundary layer vorticity generated at the wall and eject an offspring or secondary vortex. Understanding the dynamics of elementary vortex–wall interactions, which is the interest of the present study, can provide insight into mechanisms by which large-scale two-dimensional vortical structures can lead to multi-scaled highly three-dimensional flows. A well-known practical application concerns wing tip vortices generated near a ground plane, which is part of a comprehensive review by Spalart (1998). Such a pair of counter-rotating wake vortices created by an aircraft in flight can impose a significant hazard to trailing aircraft in the form of a sustained rolling moment, and provides a limit to maximum traffic that can be handled at airports. Further applications for vortex–wall interactions include the vortex structures generated by actuation of manoeuvring surfaces mounted on underwater bodies, or indeed the use of vortex generators that serve to generate streamwise vortices to manipulate turbulent boundary layers on a wing surface – see Velte, Hansen & Okluov (2009) and the review by Lin (2002).

The approach of a two-dimensional counter-rotating inviscid point vortex pair to a wall was investigated by Lamb (1932), who showed that the vortices move apart along hyperbolic trajectories. In actual measurements of flight vortex data presented by Dee & Nicholas (1968), the vortices appeared to 'rebound' as they approached the surface. This curious effect was successfully explained by Harvey & Perry (1971) and later in simulations by Peace & Riley (1983); as the vortex pair approaches the wall, a boundary layer is formed at the wall beneath each vortex of opposite-signed vorticity, which can separate to form a discrete secondary vortex. This induces an upward velocity on the original primary vortex, causing the apparent 'rebound'. Orlandi (1990) identified the possibility of multiple rebounds, each associated with an additional detachment of vorticity at the wall. A number of other two-dimensional numerical simulations have been conducted in order to explore the effects of ambient turbulence, cross-winds and stratification, many of which are discussed in the comprehensive review paper by Spalart (1998). The more recent simulations by Clercx & Bruneau (2006) and Kramer, Clercx & van Heijst (2007) have demonstrated that the evolution of small-scale vorticity at the wall can have a profound impact on the resulting dynamics, suggesting that a high resolution is needed for convergence.

As an illustration of the secondary vorticity generation from an essentially two-dimensional flow, we include in figure 1 a visualization of the interaction between an approaching vortex pair with a horizontal ground plane, using laser-induced fluorescence (LIF). We employ a technique where we mark primary and secondary vorticity with different dye sources (explained in § 2). Secondary vorticity has already separated from the wall into discrete vortices, causing the primary vortices to rebound away from the wall, as discussed above.

The study of the three-dimensional evolution of a vortex pair out of ground effect has been a topic of considerable interest due to its aerodynamic applications, in particular aircraft wake interactions. The wake vortices left behind aircraft can sometimes be observed through the condensation of water in their low-pressure cores, forming 'contrails', which can develop a symmetric waviness, with a wavelength several times that of the initial vortex spacing. Ultimately, through vortex reconnection, the flow can evolve into a periodic configuration of vortex rings. These rings can be

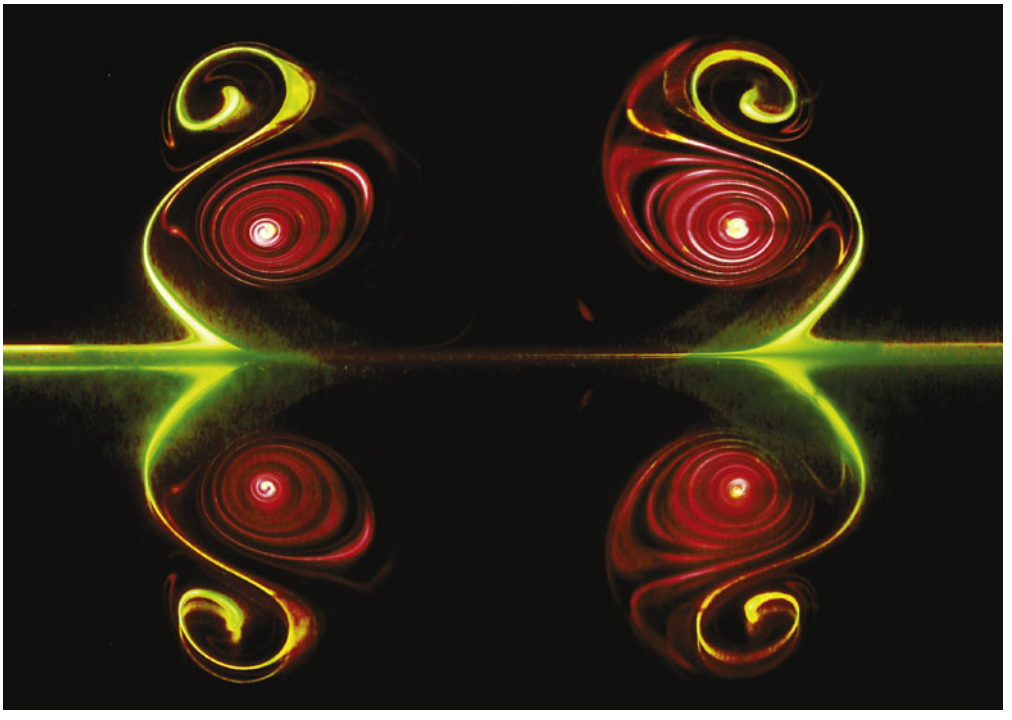

FIGURE 1. Counter-rotating vortex pair in ground effect. The primary vortices (coloured red) descend downwards under their own self-induced velocity and create a boundary layer at the wall, which can ultimately separate and form secondary vortices (green) of opposite rotation. The lower half of the image is a mirror reflection of the vortices in the polished ground plane. This particular image has appeared in the Gallery of Fluid Motion, American Physical Society (Harris, Miller & Williamson 2010).

remarkably similar in the laboratory (Leweke & Williamson 2011) to those observed in the sky at significantly higher Reynolds numbers (Crow 1970). In fact, Crow was the first to analyse the instability of a vortex pair, showing how a sinusoidal perturbation of the vortex core (moving as a whole) may grow exponentially due to the presence of the strain rate field of the neighbouring vortex. Widnall, Bliss & Tsai (1974) found that shorter wavelengths are also unstable if one considers perturbations with a more complex internal structure. They suggested that the vanishing of the rotation rate of a perturbation on the vortex core allowed the disturbance to be amplified by an externally imposed strain field. The self-induced rotation rates were originally predicted for a Rankine vortex by Kelvin (1880).

Widnall's theory corresponds well with the analysis of Moore & Saffman (1975) and Tsai & Widnall (1976), who considered a single vortex in an externally imposed strain field. Since that time, Bayly (1986), Pierrehumbert (1986) and Waleffe (1990) demonstrated that two-dimensional flows with elliptical streamlines are unstable to three-dimensional perturbations, and this is often referred to as the 'elliptic instability'. Short-wavelength instability in a vortex pair was observed experimentally by Leweke & Williamson (1998), who also demonstrated that the growth rates associated with the elliptic instability, and those higher radial modes described by Widnall *et al.* (1974), are identical in the low-strain limit, and agree surprisingly well with the modes

observed experimentally. They discovered that the flow evolves with a particular anti-phase relationship between the instabilities in the two vortices, and defined this as a 'cooperative' elliptic instability.

In order to make accurate comparisons with experiment, a continuous vorticity distribution needs to be used. Widnall, Bliss & Zalay (1971) demonstrated that the long-wave instability of a Lamb–Oseen vortex could be described by the instability of an 'equivalent' Rankine vortex. This equivalence for the long-wave instability was most recently verified experimentally by Billant, Brancher & Chomaz (1999). Leweke & Williamson (2011) considered the instability of a Lamb–Chaplygin vortex pair, finding good comparison with the experimental measurements of Leweke & Williamson (1998). The short-wave instabilities on a Lamb–Oseen vortex were also analysed by Eloy & Le Dizés (1999), and later extended to vortices of unequal strength and core size (Le Dizés & Laporte 2002), whose results are relevant to the current study.

A visual overview of the well-known instabilities for vortex pairs is shown in figure 2. In isolation from the ground, we show in figure 2(*a*) the long-wavelength Crow instability (of wavelength several times the initial vortex spacing), and in figure 2(*b*) the short-wavelength cooperative elliptic instability (of wavelength of the order of the vortex core size). These images are not shown to the same scale. The Crow instability clearly shows the bending displacement mode, whereby the vortex tube is bent as a whole, in this case in a symmetric fashion. The vortex tubes on each side of the flow reconnect to form a periodic array of vortex rings. The elliptic instability involves more detailed and complex internal deformations within the vortex tubes, and shows an antisymmetric most unstable mode. On the other hand, the secondary vortices generated by vortex–ground interactions are most unstable to an antisymmetric mode, which looks from visualization in figure 2(*c*) to be of the displacement type, where the vortex tubes are bent as a whole, at least in a low-Reynolds-number regime. It should be mentioned that, in isolation from a ground plane, a vortex pair can simultaneously exhibit the (short-wave) elliptic instability and the (long-wave) Crow instability, if the Reynolds number is sufficiently large. In the present case, we suspect that the secondary vortices created by ground interaction undergo a displacement Crow-type instability, and at sufficiently high Reynolds numbers may also exhibit an elliptic instability.

The study of the three-dimensional interaction of a vortex with a wall has also been investigated. Luton & Ragab (1997) find that the secondary vortex is unstable in the presence of the primary vortex (at $Re_\Gamma = 2196$), and it becomes wrapped around the primary vortex, forming periodic loops of vorticity. They state that the most unstable wavelength compares very well with the theory for the second radial mode of Widnall *et al.* (1974), in essence proposing that the instability of the secondary vortex is of the elliptic type, although no further evidence supports this conclusion. In deducing this result, the unequal strength of the primary and secondary vortices is not taken into account. We shall show that, in this flow, it is critical to include the additional effects of orbital rotation of the pair, which results from the unequal strength of the vortices. Additionally, Luton & Ragab (1997) scale the wavelength of the secondary vortex instability on the core size of the primary vortex, whereas we suggest that the more relevant scaling should be with the core size of the secondary vortex.

In the computational work of Moet (2003), Georges *et al.* (2006) and Duponcheel *et al.* (2009) at higher Reynolds numbers than Luton & Ragab (1997) (*Re* of the order of 10^3–10^5), there is strong evidence that the structure of the instability is indeed of elliptic instability type (second radial mode). Periodic loops of vorticity are also

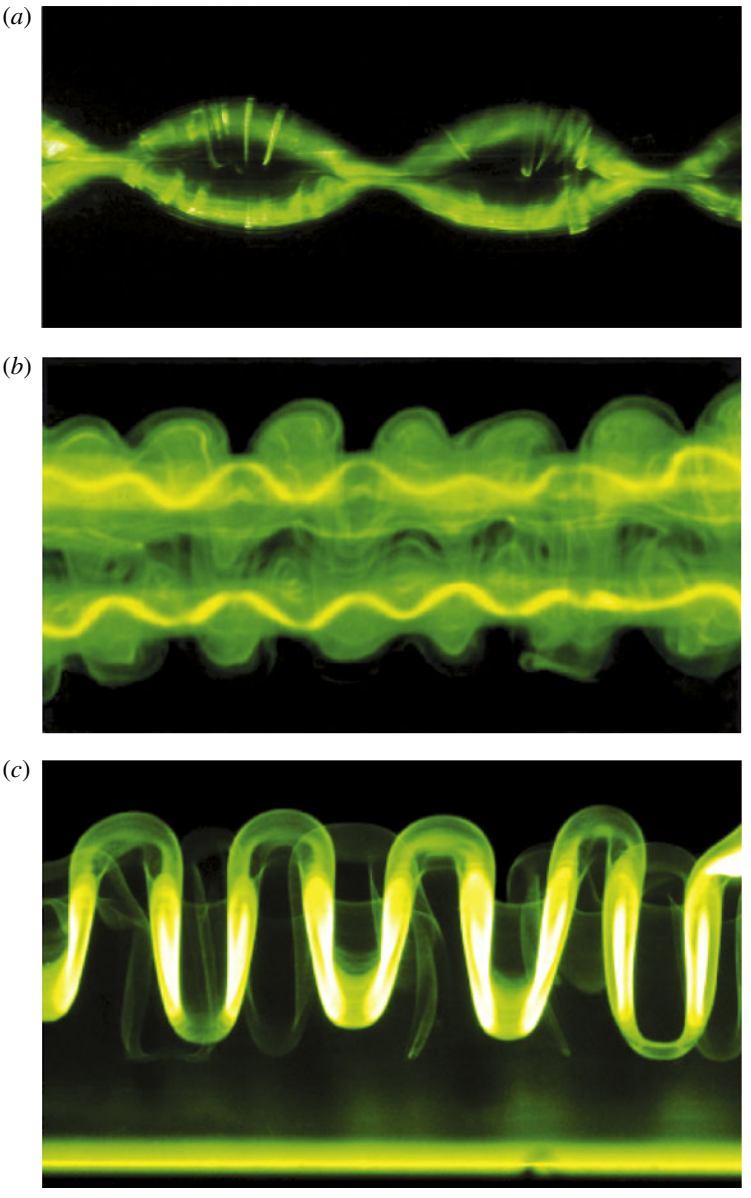

FIGURE 2. Comparisons of the principal instabilities associated with a counter-rotating vortex pair, as visualized in experiment. (*a*) Long-wave Crow instability. (*b*) Short-wave elliptic instability (Leweke & Williamson 1998). (*c*) Instability of the secondary vortices generated in ground effect; only the secondary vortices are shown here, because the primary vortices are purposely invisible, as they are not marked with dye. (Images are not to same scale.)

observed in the work of Duponcheel *et al.* (2009), although they state that the loops in their simulation originate from the outer layers of the secondary vortex, rather than the distortion of the entire secondary vortex, as we observe in the present study.

To summarize the above, in all papers that mention the source of secondary vortex instability, the origin of the instability is recognized to be of an elliptic type. However,

at least in the low-Reynolds-number regime of the present study, we shall present experimental and analytical evidence to show that it is of the displacement mode or Crow-type instability.

At this point, we introduce a whole body of research, which actually has direct relevance, but which as yet has not been associated with this problem. The flow in question has vortex pairs on each side of the wake (either co-rotating pairs, or counter-rotating pairs). Crouch (1997), and later Fabre, Jacquin & Loof (2002), have analysed the dynamics of such four-vortex flows, where a central motivation was to study whether such a vortex configuration from aircraft would break up earlier than a two-vortex wake. In the case of counter-rotating vortex pairs on either side of the wake, Ortega, Bristol & Savaş (2003) found experimentally that the weaker vortices become highly deformed, with an antisymmetric phase relationship, and that the wavelength is of the order of the initial primary vortex spacing. The weaker vortex can ultimately pinch off into vortex rings, which progress towards the stronger vortex on the opposite side of the flow. Related observations are made in the present experiments, as will be discussed later.

In subsequent analysis by Bristol, Ortega & Savaş (2004), it is shown that the instability of the four-vortex system is well represented by considering simply the isolated dynamics of one of the vortex pairs. They take account of the effect of the orbital rotation resulting from the unequal strength of the pair, which can have a significant impact on the unstable wavelength and growth of the instability. These studies are primarily concerned with trailing vortices generated from wing flaps, and also from the wing tips. However, the case comprising counter-rotating pairs on each side of the wake is remarkably similar to the problem at hand.

In the present study, we investigate the approach of a descending vortex pair to a horizontal ground plane in experiment, and rationalize our observations by analysis of the flow. Following a description of the experimental details in § 2, we follow with a presentation of the two-dimensional vortex dynamics in § 3, exhibiting the well-known phenomenon of vortex 'rebound'. In § 4, we focus on the three-dimensional instability of the flow. We find that the secondary vortices are bent as a whole in a 'displacement' mode, and, by keeping the primary vortices 'invisible' (selectively visualizing the secondaries only), we are able to see both sides of the flow simultaneously, showing that the instability perturbations on the secondary vortices are antisymmetric. In § 5, we analyse the three-dimensional instability, noting the similarity of our flow field with the recent studies on four-vortex aircraft wake flows. In contrast with previous (numerical) results for the vortex–ground interaction, which all indicate an elliptic instability, we find that the measured secondary vortex wavelength corresponds well with the displacement bending mode. We also analyse the elliptic instability modes, by employing the approximate dispersion relation of Le Dizés & Laporte (2002) in our problem, finding that the experimental wavelength is distinctly longer than predicted for the higher-order elliptic modes. However, elliptic instability is likely to occur at higher Reynolds numbers, as suggested from recent numerical studies.

Finally, in § 6, we observe that the secondary vortices deform into a distinct waviness along their lengths, and this places two rows of highly stretched vertical segments of the vortices in between the horizontal primary vortices. The two rows of alternating-sign vortices translate towards each other and ultimately merge into a single vortex row. We model these dynamics by a system of point vortices. The overall conclusions follow in § 7.

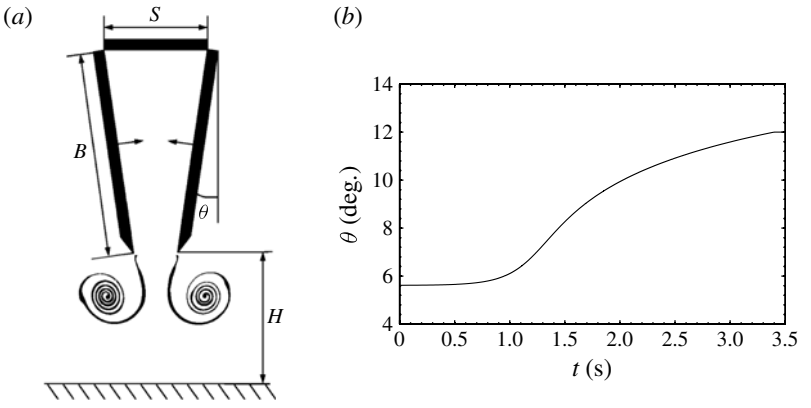

FIGURE 3. (*a*) Schematic of the vortex pair generator; $S = 5.2$ cm, $B = 10.3$ cm, $H = 6$ cm. (*b*) Angular motion of plate as a function of time, based on the motion prescribed by Leweke & Williamson (2011).

2. Experimental details

The vortex dynamics and instabilities of the present study are investigated with the vortex generator tank at Cornell University, which was originally constructed by Thomas Leweke in 1995, and is described in previous works (Leweke & Williamson 1998, 2011). The flow is investigated in a glass-walled water tank of dimensions 180 cm × 45 cm × 60 cm. The apparatus consists of two anodized aluminium plates 170 cm in length, hinged at a common horizontal base, a cross-section of which is shown in figure 3(*a*). The flaps are closed simultaneously using a computer-controlled stepper motor. As the flaps are closed, the displaced fluid between the plates is ejected vertically downwards through the gap, forming the primary vortex pair, as shown in figure 3(*a*). The motion history of the plates is presented in figure 3(*b*) and was designed by Leweke & Williamson (2011) to consistently produce uniform laminar vortex pairs. The plates were also designed so that a very small-amplitude sinusoidal perturbation could be introduced along the plate edge with an amplitude of 0.5 mm. However, the uniform (straight) plate edges were used in general for work presented, *except where explicitly noted.*

For the present study, the tank was fitted with a submerged ground plane of clear acrylic, which spans nearly the entire length of the tank. A rendering of the facility is presented in figure 4. Fogg (2001) determined a minimum height at which the vortex generation process is unaffected by the presence of the ground plane. We exceed this recommended height for the present study and we ensure that instabilities do not develop on the primary vortex pair prior to its interaction with the ground.

In order to visualize the primary vortex pair, we paint the flaps with a fluorescent dye prior to lowering the plate apparatus into the water tank. The flow is then illuminated with a 5 W argon laser and the images recorded on a high-resolution digital single-lens reflex (DSLR) camera. To distinctly mark the secondary vortices, fluorescent dye is pooled on the ground plane, prior to each experiment. This technique allows for the *visualization of the secondary vortices independently of the primary vortices* as evidenced in figure 5.

Quantitative flow measurements were made by using particle image velocimetry (PIV) using the methods described by Leweke & Williamson (1998, 2011). The fluid

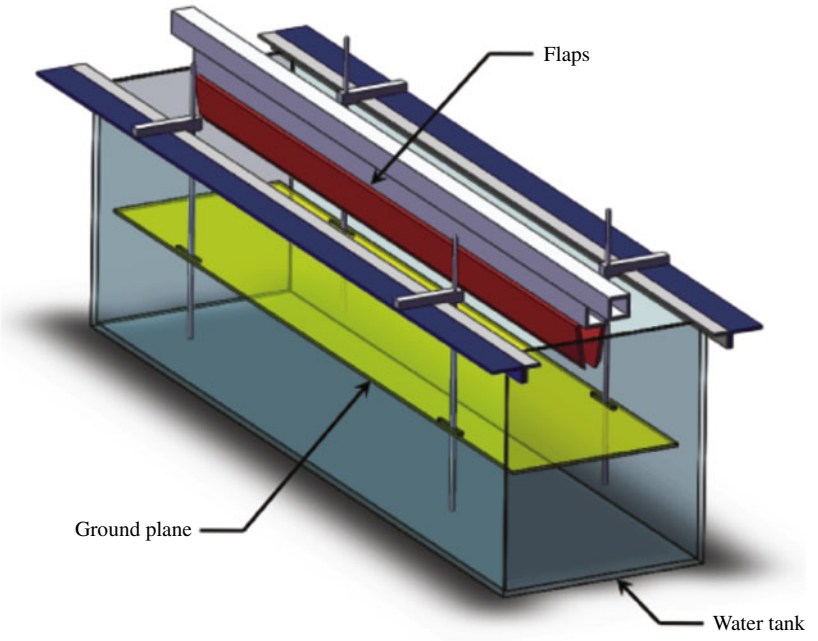

FIGURE 4. Schematic of the vortex generation facility. The original version of this facility was built by Thomas Leweke in 1995.

is seeded with micro-particles prior to the experiment (with a mean diameter of 75 μm and density of 1.03 g cm^{-3}), and we illuminate the plane of interest with a thin (3 mm) sheet of laser light. During the experiment a sequence of greyscale images are captured using a charge-coupled device (CCD) camera. Velocity fields are then calculated by processing successive images (1/30 s separation) using a multiple-step cross-correlation method incorporating window shifting, which is described extensively by Leweke & Williamson (1998). Typical image size for this study was 800 × 400 pixels (17.2 cm × 8.6 cm) with typical final velocity fields composed of 80 × 40 velocity vectors (with vectors spaced approximately 2 mm apart). Note that we present contour plots of vorticity throughout the paper only to demonstrate the qualitative evolution of the vorticity distribution, rather than any precise numerical values.

The PIV measurements allowed for the determination of the initial conditions of the flow, and the subsequent dynamics. As the vortex pair descends away from the generation mechanism, the vertical (azimuthal) velocity is measured along a horizontal line passing through the centres of the vortices. The measured velocity profile is well described by the superposition of two Lamb–Oseen vortices (Gaussian distribution of vorticity), each with the azimuthal velocity profile

$$v_\phi(r) = \frac{\Gamma}{2\pi r}\left[1 - \exp\left(-\frac{r^2}{a^2}\right)\right], \tag{2.1}$$

where Γ is the circulation of the vortex, r is the distance from the centre, and a is a distance characterizing the core size of the vortex. A least-squares best-fit method, following Leweke & Williamson (1998), is performed to determine the initial circulation (Γ_o) and core size (a_o), as well as the initial vortex spacing (b_o).

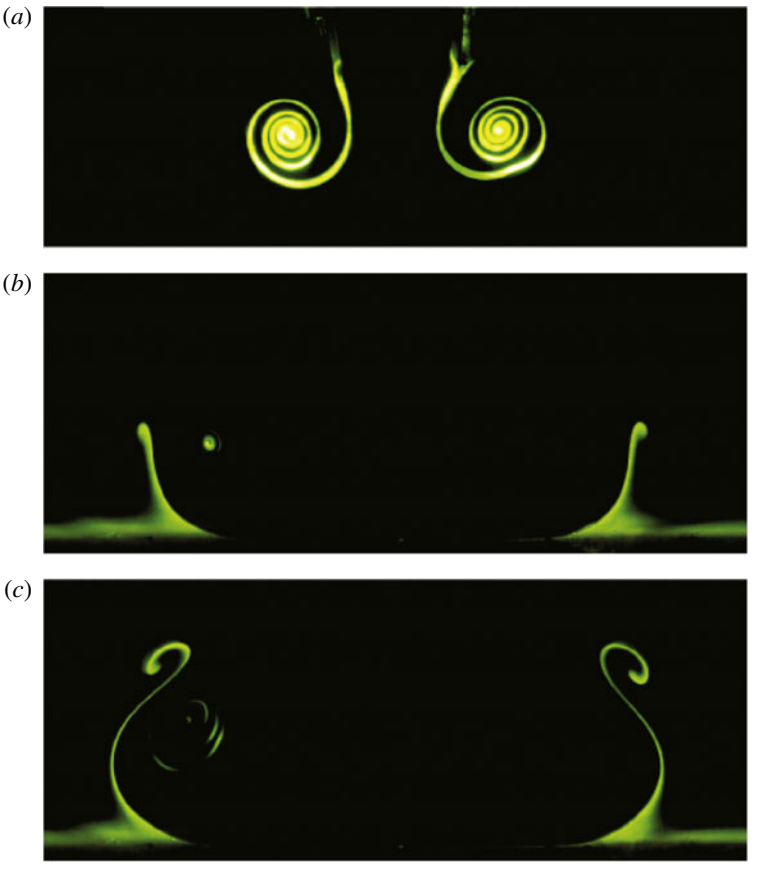

FIGURE 5. Demonstration of the selective visualization of primary or secondary vortices. (*a*) Visualization of primary vorticity generated at flap edges during vortex generation process. (*b*,*c*) Visualization of secondary vorticity (separated from the wall boundary layer), while keeping the primary vortices invisible. A small amount of residual dye remained on the left flap, resulting in a faint left primary vortex.

An example of such a fit is shown in figure 6(*a*). Typical measurements for this investigation are $b_o = 1.7$ cm and $a_o/b = 0.35$. The associated Reynolds number of the flow is defined as $Re = \Gamma_o/\nu$, where ν is the kinematic viscosity of the water. The Reynolds number can be varied by changing the overall duration of the flap motion (up to $Re \approx 3000$).

A non-dimensional time t^* for the evolution of the primary vortices is defined by

$$t^* = t\frac{\Gamma_o}{2\pi b_o^2}. \tag{2.2}$$

We define the origin of the time ($t^* = 0$) to be when the height of the descending vortex pair reaches 3.5 cm or approximately $2b_o$ above the ground plane. The vortices are at this height after the generation process is complete, but before the ground interaction significantly affects their trajectories.

We define d as the measurement of the distance between the primary and secondary vortices, a_1 and a_2 to represent their respective core sizes, and Γ_1 and Γ_2 to represent

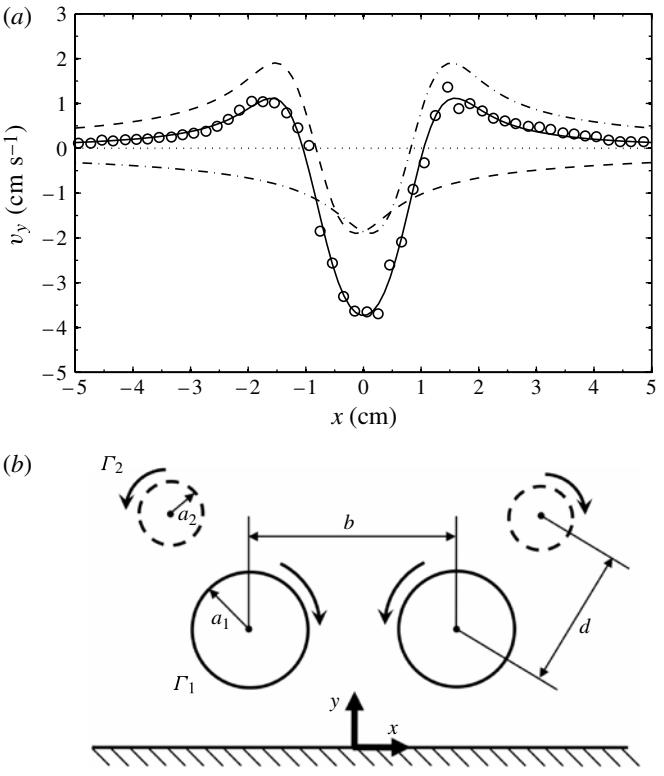

FIGURE 6. (*a*) Least-squares fit of azimuthal velocities of two superposed Lamb–Oseen vortices (——), profile of independent Lamb–Oseen vortices (left, – –; right, – · –) with sample vertical velocity data at a line passing through the vortex centres (○). (*b*) Schematic of observed flow and definition of parameters. Solid circles represent the primary vortices, whereas the dashed circles represent the secondary vortices.

their circulations, as shown in figure 6(*b*). Defining a core size of the evolving secondary vortex is not straightforward, however, so we use the estimate suggested by Duponcheel *et al.* (2009) in their numerical study of the same flow. This estimate takes circular contours of integration centred on the secondary vortex and determines the azimuthal velocity of an axisymmetric vortex with an equivalent circulation. The radius at which this velocity is a maximum is taken to be an estimate of the core size of the secondary vortex:

$$v_{\phi,max} = v_\phi(r_c) = \max_r \left(\frac{\Gamma(r)}{2\pi r} \right). \tag{2.3}$$

Applying the above to an axisymmetric Lamb–Oseen vortex equation (2.1) yields

$$r_c = 1.12a. \tag{2.4}$$

For the case of the secondary vortex, we use this equation to relate the measured radius of maximum velocity r_c to the parameter a where needed.

Additionally, we have characterized the error of the parameter measurements by performing five independent experiments with identical flap motion and assessing the variation in the measured quantities derived from the PIV data. This test was

conducted at various Reynolds numbers spanning our range of interest, and the results were consistent between tests. This method yielded typical uncertainties for the initial conditions of the flow calculated from the Lamb–Oseen fit as $\Delta\Gamma_o/\Gamma_o \approx 4\,\%$, $\Delta b_o/b_o \approx 5\,\%$ and $\Delta a_o/a_o \approx 5\,\%$. When wavy perturbations (of amplitude 0.5 mm) to the flap edges are introduced (only when explicitly noted), the measured initial parameters of the flow fall within the uncertainties reported above, indicating that the vortex generation process is largely unaffected by the introduction of the very small-amplitude perturbations.

The calculation of vorticity fields is subject to error in analysis; in general, the peak vorticity values are reduced as the level of smoothing is increased. In order to calculate the circulation values Γ_1, Γ_s and Γ_2, a line integral is calculated using an interpolated velocity field over a specified integration contour. The circulation value was only weakly sensitive to the level of smoothing, as vorticity magnitude is not used in the computation. Typical uncertainties in circulations are $\Delta\Gamma_1/\Gamma_1 \approx 4\,\%$, $\Delta\Gamma_s/\Gamma_s \approx 10\,\%$ and $\Delta\Gamma_2/\Gamma_2 \approx 10\,\%$.

The reported secondary vortex core size (r_c) and primary to secondary vortex spacing (d) is taken at the time when the secondary vortex circulation (Γ_2) reaches a maximum, with a typical uncertainty of $\Delta r_c/r_c \approx 10\,\%$ and $\Delta d/d \approx 10\,\%$. Instability wavelengths of the secondary vortex (λ) were measured directly from the digital images enlarged in image processing software. Variation in the measured wavelength (within a single experiment and over many experiments) was $\Delta\lambda/\lambda \approx 20\,\%$, which reflects a somewhat broad spectrum of unstable wavelengths.

3. Two-dimensional vortex–wall interaction

In this section, we shall characterize the dynamics of the two-dimensional vorticity, as the primary vortices interact with the ground plane. It is essential to understand the two-dimensional flow prior to studying the three-dimensional instabilities of the vortices.

The evolution of the flow at a low Reynolds number ($Re = 1260$) is shown in figure 7, using LIF in a cross-section cutting through the axes of the vortices, as well as using digital PIV measurements to determine vorticity at the times corresponding to the flow visualization images. The primary vortex pair translates vertically downwards from the flaps (see $t^* = 1.0$), and a boundary layer starts to develop along the ground plane under each vortex. The layer of opposite vorticity is subjected to an adverse pressure gradient, separates from the wall ($t^* = 2.7$) and begins to induce an upward velocity on the primary vortex pair, leading to the well-known 'rebound' of the primary vortices ($t^* = 4.0$). A discrete secondary vortex sheds, and is advected around the stronger primary vortex ($t^* = 5.0$). As the secondary vortices reach the region in between the primary pair, they begin to lose their once coherent structure in the cross-sectional view ($t^* = 6.4$), and the flow becomes highly three-dimensional. An additional weaker secondary vortex is formed at this time, and the rebound process will repeat itself, although in a weaker fashion, as will be seen below.

The trajectory of the primary vortex pair is measured from the flow visualization, and a typical trajectory is displayed in figure 8, showing clearly the vortex rebound phenomenon, as originally explained by Harvey & Perry (1971). The solid lines are the hyperbolic trajectories of a pair of point vortices, originally deduced by Lamb (1932). The secondary vortices orbit the primary vortices, as a result of their unequal strength, and the primary vortices follow a spiral trajectory. We observe a second rebound, which is associated with the generation of an additional secondary vortex,

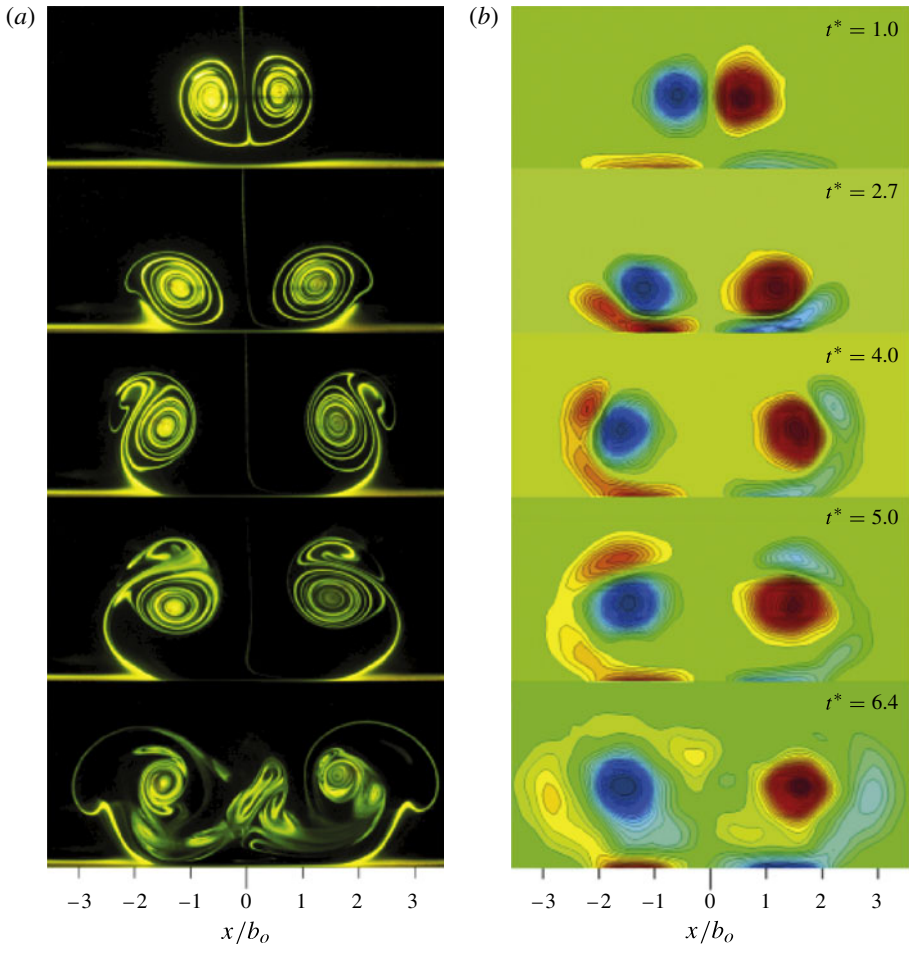

FIGURE 7. Evolution of a counter-rotating vortex pair in ground effect ($Re = 1260$) from (*a*) flow visualization and (*b*) vorticity contours from PIV data. Normalized times (t^*) during experiment of adjacent images are the same. The PIV vorticity contour plots in panel (*b*) are only meant to demonstrate the qualitative evolution of the vorticity distribution, rather than any precise numerical values. The vorticity contour levels are redefined at each time step.

as mentioned earlier. During the early stages of the experiment, when the flow is still effectively two-dimensional, the trajectories are highly reproducible in each experiment. Once three-dimensional effects dominate the flow, the trajectories can become slightly asymmetric, with more variability, as might be expected, although the general qualitative features persist.

The generation of a secondary vortex and the possibility of multiple rebounds are consistent with the results of the numerical simulations of Orlandi (1990) at Reynolds numbers of the order of 10^3. He noted that a well-resolved simulation of this flow requires a high spatial resolution to achieve grid independence. More recently, careful numerical investigations over a range of Reynolds numbers ($O(10^2$–$10^4)$) have been conducted by Clercx & Bruneau (2006) and Kramer *et al.* (2007) in which very similar phenomena are observed. They also observe multiple rebounds of the primary

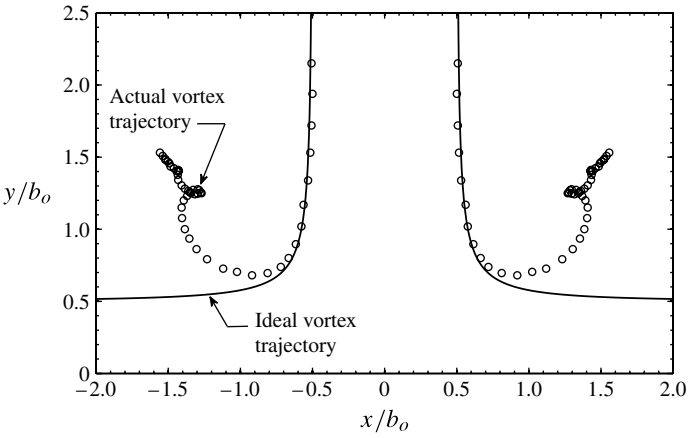

FIGURE 8. Primary vortex trajectories (○) as measured in experiment compared with hyperbolic trajectory (—) of a point vortex pair approaching a horizontal boundary, as deduced by Lamb (1932).

vortices, but the amplitude of the later rebounds is greater than observed in the present experiments. This is probably due to additional three-dimensional effects (in the experiments), which can lead to an enhanced dissipation of the flow. They found that small-scale vorticity generated at the wall can dramatically affect the resulting dynamics, thus requiring a high resolution for convergence. They conclude that this seemingly simple two-dimensional flow is actually extremely difficult to compute, and simulations must be done with care. It is additionally proposed that this particular flow be used for a benchmarking tool to evaluate future numerical algorithms. This problem was also simulated by Türk, Coors & Jacob (1999) up to a much higher Reynolds number ($O(10^2$–$10^6)$), with some similar results, although it is probable that some critical small-scale structures would not be resolved owing to the high Reynolds numbers.

To further characterize the two-dimensional flow field development, we show in figure 11(*a*) the time evolution of the height of the primary vortex above the ground plane. Correspondingly, in figure 11(*b*) we find the evolution of the primary vortex strength (Γ_1), the entire secondary vorticity including the wall vorticity (Γ_s) and the discrete secondary vortex as it evolves in time (Γ_2) for a sample experiment. We have included a few typical error bars (based on the error discussion in § 2). The shedding of a discrete secondary vortex represents the vorticity, which has a distinct peak of its own away from the wall vorticity. (A measure of Γ_2 is given as follows. We find the locus of points marking the maximum secondary vorticity at each height above the wall. Along that locus, as a discrete vortex forms, there will be a minimum, and above this minimum we integrate the secondary vorticity to determine the vortex strength, Γ_2.) An essential point to note here is that the primary rebound starts around the time that the discrete secondary vortex (Γ_2) sheds from the ground vorticity (Γ_s) at the time ($t^* \approx 2$). At the same point, the circulation of the primary vortex starts to decay as a result of mixing and diffusion.

As the Reynolds number is increased in figure 10 to $Re = 2150$, the secondary vortex is shed more rapidly from the wall vorticity. The increased evidence of non-symmetric vorticity in these images suggests that three-dimensionality develops earlier in the orbit of the secondary vortex. In particular, in the visualization of figure 10, at

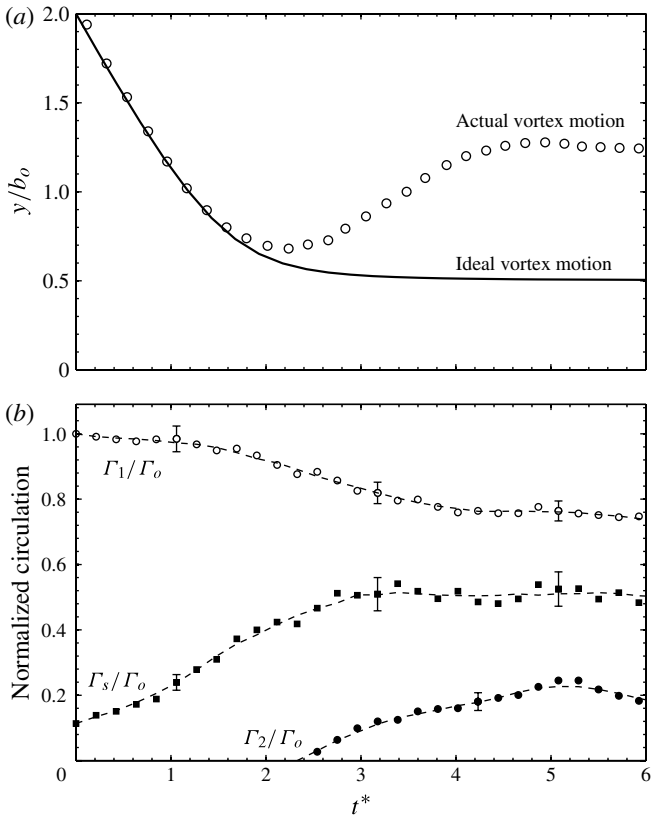

FIGURE 9. (*a*) Mean height of primary vortex pair above wall versus time. Rebound occurs at $t^* \approx 2$. (*b*) Time evolution of mean primary vortex circulation (Γ_1), total secondary circulation (Γ_s) and circulation of shed secondary vortex (Γ_2). Circulations are normalized by initial primary vortex strength, Γ_o. A few typical error bars are shown.

time $t^* = 4.8$, we can see that the left-side secondary vortex is separating from the primary vortex, while the right-side secondary vortex is moving closer to the primary vortex. Apparently, there is a tendency for the secondary vortex instabilities to be out of phase on each side of the flow field, even at this stage. This kind of phase relationship is a common feature of the secondary vortex instability, as will be seen later in the paper, from different views of the flow.

Finally, we show the variation of the core size and the strength of the secondary vortex versus Reynolds number in figure 11. We have included a few typical error bars (based on the error discussion in § 2). The core size gradually decreases as the Reynolds number increases, which might be expected since diffusion becomes less significant as the secondary vortex is advected around the primary vortex. The trend suggested by our experimental data agrees favourably with the simulation results at higher *Re* of Duponcheel *et al.* (2009), and is presented in figure 11(*a*). To examine the secondary vortex strength, we include data from the two-dimensional numerical simulations of Gupta (2003), as well as data from the simulations of Kramer *et al.* (2007) to yield a plot of data in figure 11(*b*). It is important to note that the definition of Reynolds number given in Kramer *et al.* (2007) differs from that of the current work, and thus an equivalent Reynolds number must be estimated. The complete data

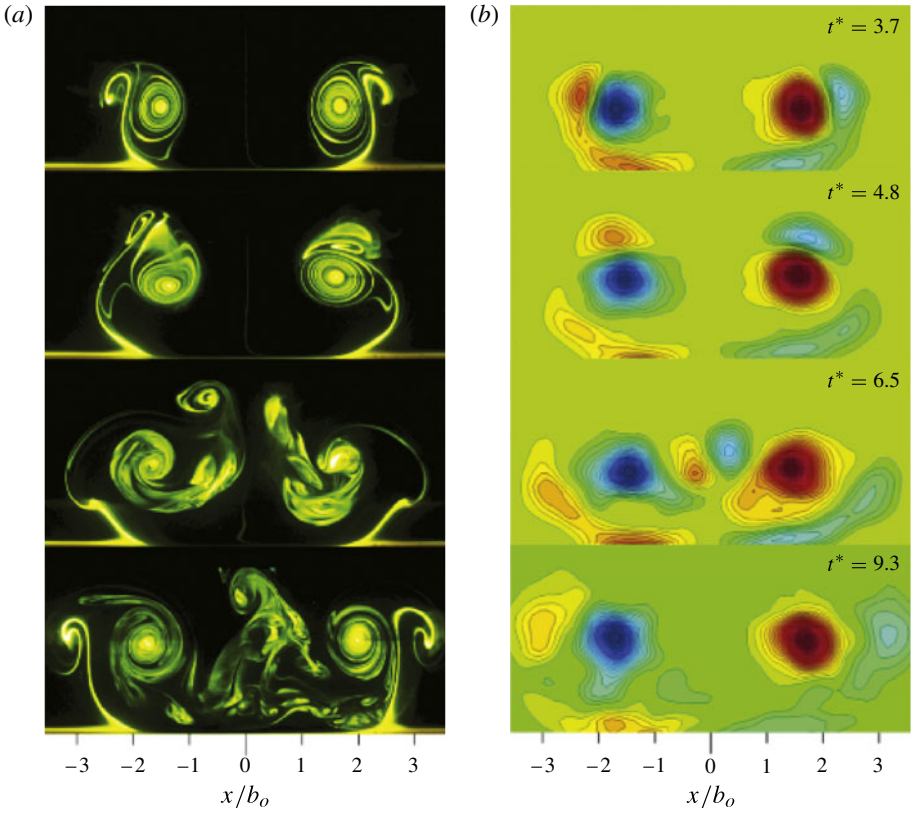

FIGURE 10. Evolution of a counter-rotating vortex pair in ground effect ($Re = 2150$) from (*a*) flow visualization and (*b*) vorticity contours from PIV data. Note the earlier loss of symmetry and more discrete secondary vortex as compared to the lower *Re* experiment shown in figure 7. The vorticity contour levels in panel (*b*) are redefined at each time step; the measurements are only intended to demonstrate the qualitative evolution of vorticity.

are well fitted by the linear relation

$$\frac{\Gamma_2}{\nu} = c(Re - Re_c), \tag{3.1}$$

where $c = 0.41$ and $Re_c = 430$.

Interestingly, the presence of an offset along the *Re* axis suggests a critical Reynolds number, Re_c, below which one might expect that a discrete secondary vortex is not formed. A second interesting feature about the form of equation (3.1) is that it suggests that the strength ratio of Γ_2/Γ_o asymptotes to a value c in the limit of high *Re*, which becomes more apparent in the presentation of the data in figure 11(*c*). We do not expect this to hold for all *Re*, as turbulent effects will become increasingly important for high Reynolds numbers.

4. Three-dimensional instability of the secondary vortices

In this section we characterize the three-dimensional development of the flow, which manifests itself even in the two-dimensional cross-sectional images in figure 7. To explore the precise nature of the three-dimensionality, we use the same dye

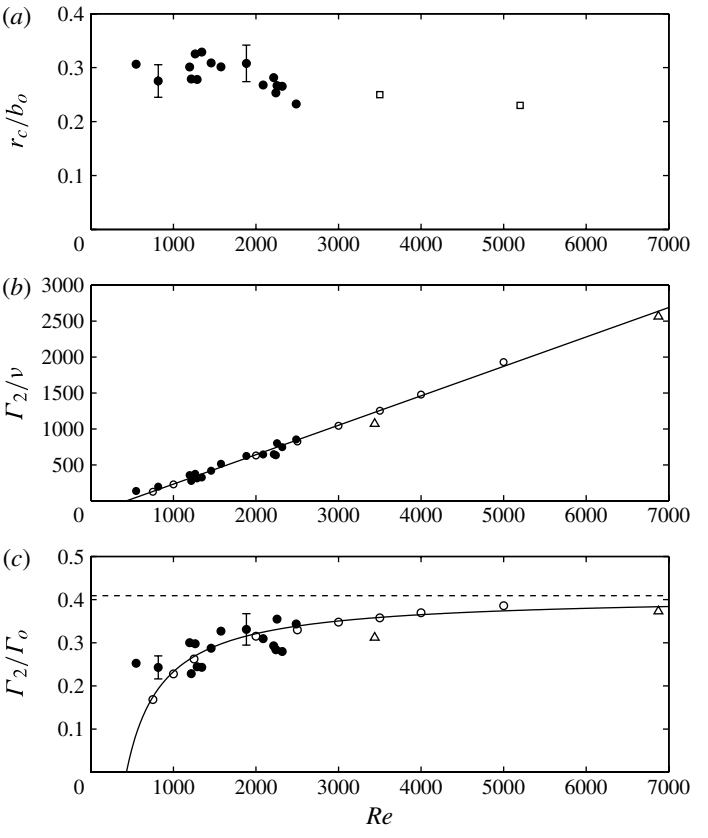

FIGURE 11. (*a*) Secondary vortex core size versus *Re*: •, present experiments; □, Duponcheel *et al.* (2009). (*b*) Secondary vortex strength versus *Re*: •, present experiments; ○, Gupta (2003); △, Kramer *et al.* (2007); with fitted curve (—) of form specified by (3.1). (*c*) Ratio of secondary vortex strength to initial primary vortex strength versus *Re*: the dashed line represents the asymptotic limit of strength ratio suggested by best fitting using the form of (3.1).

visualization techniques as presented in § 2, but in this case we illuminate the entire flow as well as cross-sections. In this and all further sections, we consider the case where $Re = 1260$. We find that the secondary vortex develops a waviness as it orbits around the stronger primary vortex, as observed by previous simulations. In order to appreciate what we shall study in the visualizations, we show a qualitative three-dimensional rendering of the observed flow in figure 12(*a*). The secondary vortices become strongly deformed in a sinuous fashion between the primary vortices, after they have been advected around the primary vortices. We have also illustrated the anti-phase relationship between the sinuous perturbation on each of the secondary vortices, which will become clear in the flow visualizations below.

We first visualize the flow in figure 13(*a*) from the same perspective as in the two-dimensional investigation, and we find that the secondary vortex structure has been reoriented such that the principal vorticity lies along the circumference of the primary vortex. To gain insight into the nature of the three-dimensionality, we visualize the flow from above in figure 13(*b*) and from the side in figure 13(*c*). It is now clear that

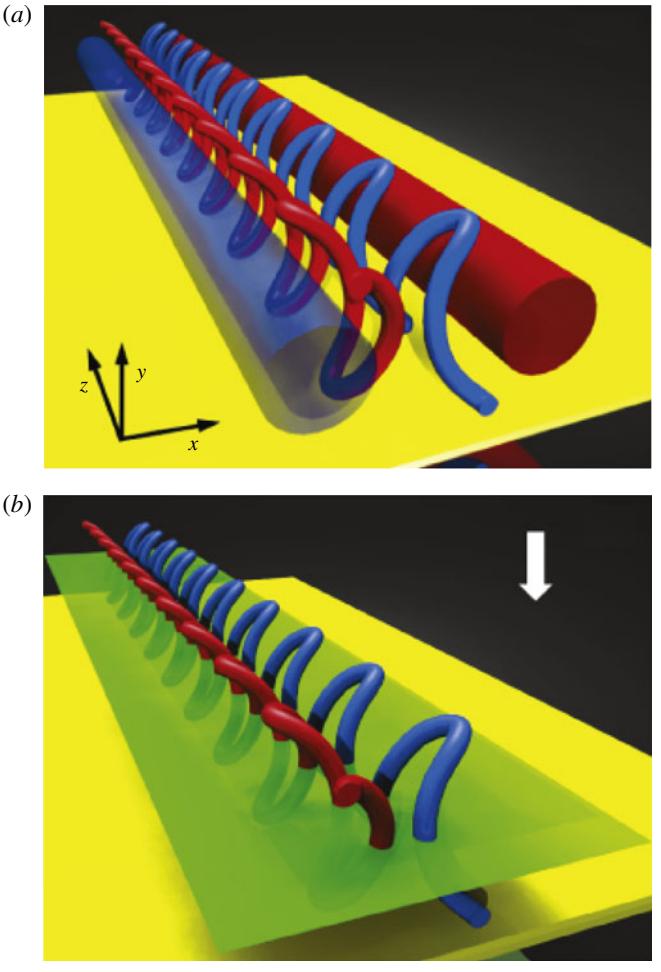

FIGURE 12. Colour rendering of the qualitative features of the three-dimensional flow. (*a*) Secondary vortices are shown as highly deformed thin tubes in between primary vortices, which are represented by undeformed thick tubes. The yellow plane represents the ground. (*b*) Secondary vortices only, with sheet of laser light shown as the green plane parallel to ground.

periodic structures have emerged from the once straight secondary vortex. Figure 13(*c*) shows the flow during the incipient stages of the instability, as the secondary vortex is roughly above the primary vortex.

Using the dye visualization technique as described in § 2, we selectively mark only the secondary vortices with dye, rather than the primaries. Images taken from three different experiments are presented in figure 14. The secondary vortices are between the primary vortices (which are invisible), demonstrating the value in the ability to observe the secondary vortices exclusively. We find an antisymmetric phase relationship in the instability of the secondary vortices in all experiments, suggesting the action of a cooperative instability. As most evident in figure 14(*a*), we observe a range of unstable wavelengths along the secondary vortex, in all of

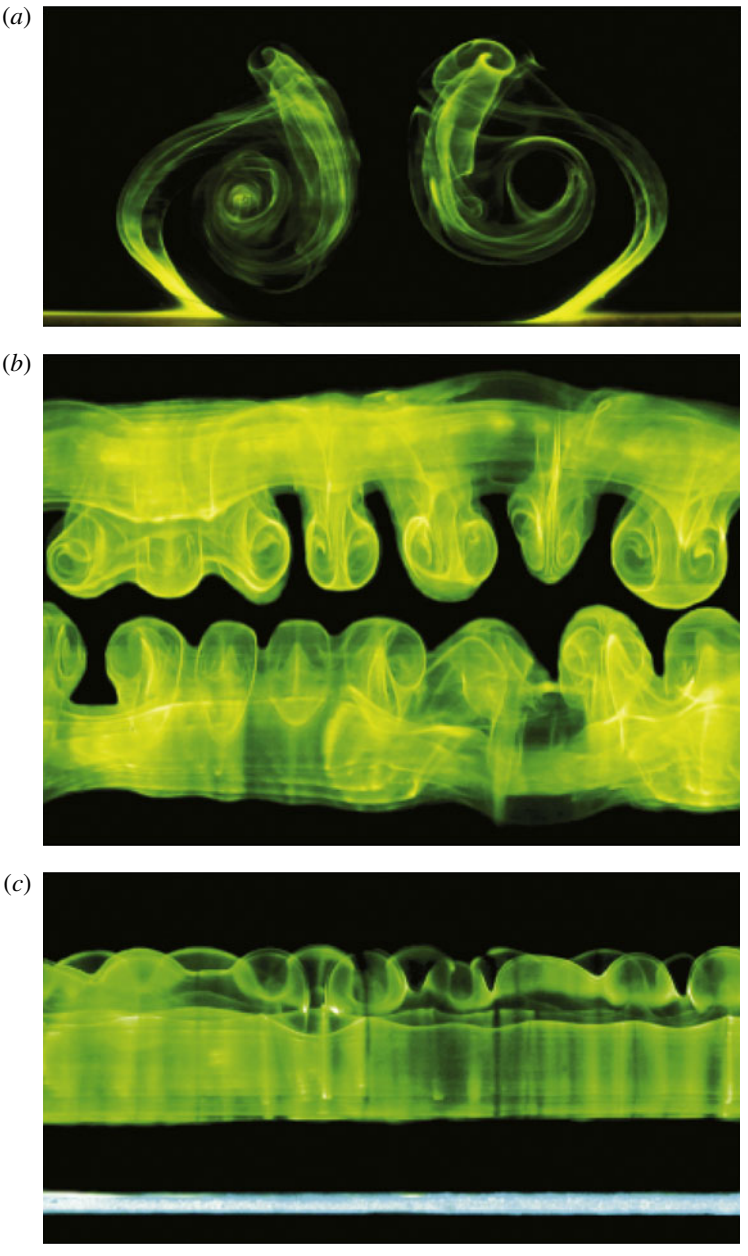

FIGURE 13. Three orthogonal views of the fully illuminated three-dimensional flow. (*a*) Axial view, same perspective as images in figure 7. (*b*) Top view as secondary vortices pass between primary vortices. (*c*) Side view of incipient instability of secondary vortices as they pass just above the primary vortices. Note the distinct antisymmetric phase relationship of the instability in panels (*b*) and (*c*).

the experiments. Remarkably, the antisymmetric phase relationship of the secondary vortices uniformly persists despite this variance. The variation in wavelength, and the location of the maxima in the perturbations along the secondary vortices, was random

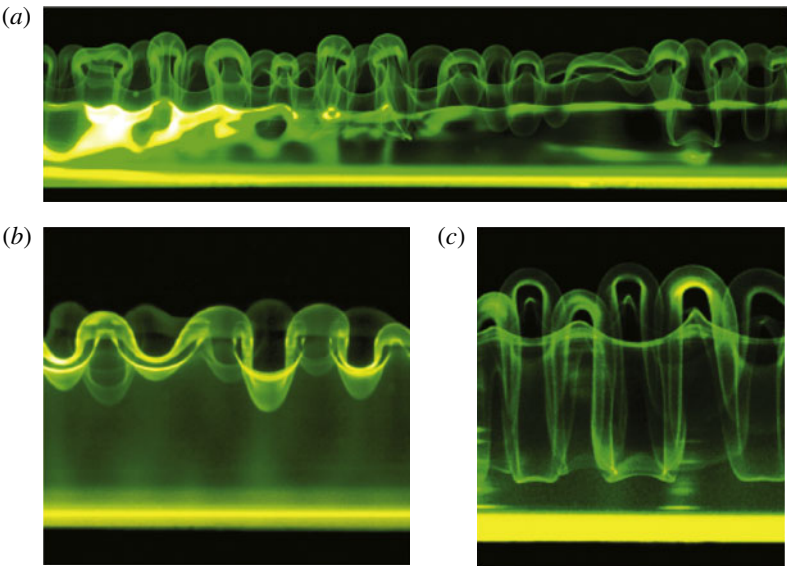

FIGURE 14. Visualization of secondary vortices only, with the primary vortices remaining invisible. The images are each from different experiments with the same initial conditions. (*a*) Demonstration that there is some range of unstable numbers, indicating that the instability mechanism has a range of wavelength selection. The antisymmetric phase relationship persists despite the fluctuation in wavelength. (*b*,*c*) Additional visualizations focusing on the highly deformed secondary vortices, again demonstrating the observed phase relationship.

between experiments, suggesting that the instability responds to ambient background perturbations in the fluid rather than some feature of the experimental apparatus.

To visualize the instability of the secondary vortices with further clarity, we introduce very small-amplitude sinusoidal perturbations to the edges of the flaps. This method is similar to that used by Leweke & Williamson (2011) for their investigation of long-wave instabilities of an isolated vortex pair. The series of images in figure 15 display the evolution of the instability using this method. The structure and development of the instability remain nearly identical to those of the unperturbed case, but the period is more regular. What is perhaps most remarkable about these experiments is that the antisymmetric phase relationship was observed *regardless of the relative phase of the initial perturbations*. This suggests that the specific instability mechanism observed in the present flow is quite robust. The initial phase of the flap perturbations for the specific experiment shown in figure 15 differed by 90°, and thus were neither symmetric nor antisymmetric.

Although not apparent in the present images, the vertical segments of vorticity on either half of the flow field, between the primary vortices, move in towards each other, away from their parent primary vortex. Simultaneously, the lower horizontal segments, which connect each vertical tube, become tightly wound around the primary vortex.

These observations are similar to recent work with a four-vortex wing wake, in isolation of any ground plane (Ortega *et al.* 2003). They observe that the weaker vortex (which is generated from a wing flap in their case) becomes highly deformed in a similar antisymmetric phase relationship, between the wing tip vortices. The flap vortices (equivalent to our secondary vortices here) eventually break apart into

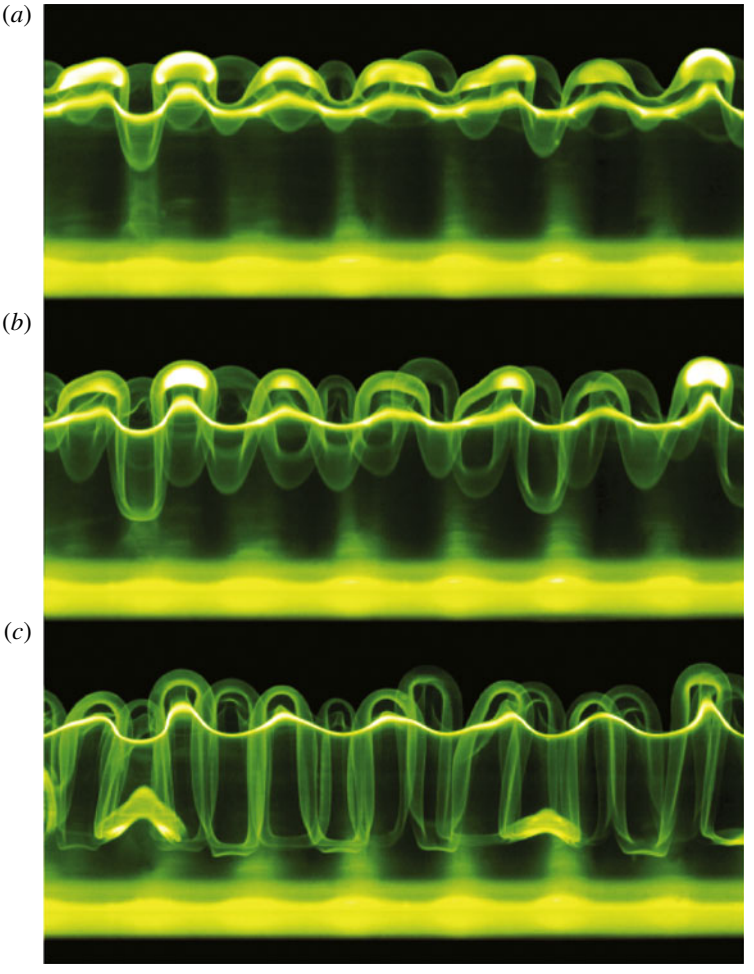

FIGURE 15. In these experiments, we have introduced a very small-amplitude (0.5 mm) sinusoidal perturbation at the flap tips. (*a*) The secondary vortices are beginning their descent between the primary vortices; the instability has already begun to develop. (*b*) The secondary vortices are advected further by the primary vortices. (*c*) Secondary vortices have evolved into nearly vertical vortex segments connected by short horizontal vortex segments. In the experiment shown, the relative phase of the initial perturbations is neither symmetric nor antisymmetric, but rather differ by 90°.

two distinct rows of periodic vortex rings, which move in towards each other. In calculations of the stability of the four-vortex system, Fabre *et al.* (2002) found that the most unstable mode, for cases where the flap vortex was much weaker than the tip vortex, has an antisymmetric phase relationship with a short wavelength, which primarily develops on the weaker vortex. Our observed flow is also quite similar to the instability of secondary vortices identified in the simulation results of Luton & Ragab (1997). However, their simulation employed a symmetric boundary condition such that only half of the flow was simulated, not allowing for the observation of a phase relationship of the instability.

5. Origin of three-dimensional instability

In this section, we shall analyse the instability of a vortex pair interacting with a wall, with the intent to determine the origin, and most unstable wavelength, of the secondary vortex instability in the presence of the primary vortex. The essential flow in question is represented in figure 6(*b*), and is very similar to the four-vortex flow analysed by Bristol *et al.* (2004) representing an aircraft wake, in the absence of a ground plane. Bristol *et al.* found that an analysis that examined only half of the flow in figure 6(*b*) (the counter-rotating unequal-strength vortex pair in isolation, in the right half-plane, for example) could accurately represent the instability of the secondary vortex in the complete flow field. We shall utilize and extend their stability analysis for the four-vortex aircraft wake configuration to our case of the vortex pair interacting with a wall. Hitherto, the realization of the similarities between these two flows has not been made, and we shall find the approach of Bristol *et al.* to yield good predictions of instability in our flow.

The early work of Crow (1970) and Widnall *et al.* (1974) analysed the instability of an equal-strength vortex pair. In essence, the physical key to analysing stability in this case is to understand that, for instability, the plane containing the sinuous perturbation (along the vortex axis) needs to be frozen in the extensional strain rate field of the neighbouring vortex, subsequently leading to exponential growth. For this to happen, the self-induced rotation (about the vortex axis) of the wave within the vortex needs to be balanced by the effect of the mean strain rate field from the neighbouring vortex as well as the effect on rotation due to the perturbation flow field of the neighbouring vortex, which is not in general insignificant. However, a principal contribution from Bristol *et al.* (2004) is to recognize that a further effect comes into play when the counter-rotating vortices have unequal strength. An extra term that serves to rotate the perturbation has to be added to the analysis of Crow, namely the angular speed of the unequal vortex pair, as they rotate around one another.

We shall follow the analysis of Bristol *et al.* (2004) in the following section, and bring their analysis to bear on our flow problem. However, it should be noted that they only analysed the displacement bending mode instability for unequal counter-rotating vortices. We therefore extend this analysis to higher modes such as the elliptic instability modes by making use of an approximate dispersion relation for Kelvin modes on the Lamb–Oseen vortex, as deduced by Le Dizés & Laporte (2002). We are able to confirm our approach with good agreement between our analysis and some very recent simulation results of So, Ryan & Sheard (2011). We then compare the experimental measurements of instability wavelength of the secondary vortices with the most unstable wavelengths coming from our analysis, which will provide evidence of the origin of our instability.

5.1. *Linear stability analysis of an unequal-strength counter-rotating pair*

If we wish to examine the stability of the weaker vortex in the presence of the stronger vortex, we define a time scale for the instability as

$$\tau = \frac{2\pi d^2}{\Gamma_1}. \tag{5.1}$$

We also define a parameter Λ that represents the relative strength of the weaker vortex (vortex 2) to the stronger vortex (vortex 1),

$$\Lambda \equiv \frac{\Gamma_2}{\Gamma_1}, \tag{5.2}$$

which will be negative for counter-rotating vortex pairs. The special case where $\Lambda = -1$ corresponds to the equal-strength pair as examined by Crow (1970) and Widnall *et al.* (1974). It can also be shown that for $a \ll d$ the vortices orbit around their vorticity centroid at the angular rate

$$\Omega = \frac{1+\Lambda}{\tau}. \tag{5.3}$$

The plane normal to the axis of each vortex we define as the x–y plane, while the direction parallel to the axis of the vortex we shall refer to as the z direction. Then, (x_i, y_i) gives the location of the centre of the vortex in some plane of constant z, where i refers to vortices 1 and 2. The unperturbed location of the vortex centre for vortex i is located at $(x_i = 0, y_i = 0)$. Following the analysis of Crow (1970) and the extension by Bristol *et al.* (2004), we sinusoidally perturb the location of the core of each vortex in the radial direction. The perturbations are given by

$$\hat{\boldsymbol{r}}_i = \boldsymbol{r}_i \exp\left(\alpha \frac{t}{\tau} + \mathrm{i}kz_i\right), \tag{5.4}$$

where α is the non-dimensional complex growth rate and k is the axial wavenumber. Note that $\boldsymbol{r}_i = (x_i, y_i)$ and are allowed to be complex. The perturbation is unstable when the real part of α is positive. We do not lose any generality in assuming the above form of the perturbations, as any arbitrary function can be recovered through superposition of these modes using Fourier analysis. Assuming that the perturbations are small, the linearized problem reduces to solving the following eigenvalue problem:

$$\alpha\hat{x}_1 = -\Lambda\hat{y}_1 + \Lambda\psi\hat{y}_2 + \sigma_1\tau\hat{y}_1 \quad + \Omega\tau\hat{y}_1, \tag{5.5a}$$

$$\alpha\hat{y}_1 = -\Lambda\hat{x}_1 + \Lambda\chi\hat{x}_2 - \sigma_1\tau\hat{x}_1 \quad - \Omega\tau\hat{x}_1, \tag{5.5b}$$

$$\alpha\hat{x}_2 = -\hat{y}_2 \quad + \psi\hat{x}_2 \quad + \Lambda\sigma_2\tau\hat{x}_2 + \Omega\tau\hat{y}_2, \tag{5.5c}$$

$$\alpha\hat{y}_2 = -\hat{x}_2 \quad + \chi\hat{x}_1 \quad - \Lambda\sigma_2\tau\hat{x}_2 - \Omega\tau\hat{x}_2. \tag{5.5d}$$

These equations describe the evolution of perturbations on a vortex pair in a rotating frame of reference, so that the orientation of the pair appears stationary. In the manner of Crow (1970) and Bristol *et al.* (2004), we describe here the physical significance of each of the terms in the above equations. Terms of similar physical relevance are aligned in vertical columns. The column on the left-hand side represents the normalized exponential growth rate of the perturbations, α. The first term on the right-hand side represents the effect from the mean strain rate of the neighbouring vortex. A vortex is exposed to a field of pure strain due to the presence of the neighbouring vortex. The primary extensional axis of the field is at a 45° angle from the line connecting the two vortices, and thus, when the perturbations are frozen close to this plane of maximal stretching, the perturbations can grow exponentially in amplitude.

If this were the only term considered on the right-hand side, the flow would be unstable for all wavenumbers, with a growth rate equal to the extensional strain imposed by the neighbouring vortex ($\alpha = 1$). The second term represents the alterations of the imposed velocity field due to the perturbations of the neighbouring vortex. The forms of these terms, often referred to as the mutual induction terms, are presented by Crow as

$$\chi(\beta) = \beta \mathrm{K}_1(\beta), \tag{5.6}$$

$$\psi(\beta) = \beta^2 \mathrm{K}_0(\beta) + \beta \mathrm{K}_1(\beta), \tag{5.7}$$

where $\beta = kd$, and $K_0(\beta)$ and $K_1(\beta)$ are modified Bessel functions of the second kind. A few key observations can be made. For very short wavelengths ($\beta \to \infty$), both mutual induction functions, χ and ψ, tend to vanish. In this limit, the combined effects of the short-wave perturbations on the neighbouring vortex tend to cancel out. However, in the long-wave limit ($\beta \to 0$), the mutual induction functions approach unity, which represents a shift in the effective origin of the strain rate field imposed by the neighbouring vortex. For long waves, this effect is of the same order as the effects of the strain rate field.

The third term on the right-hand side of (5.5) represents the self-induced rotation of the vortex core due to its own perturbations, deduced by Kelvin (1880) for the Rankine vortex, and commonly called Kelvin waves. Crow (1970) used a cut-off method to calculate this self-induced rotation rate, which is valid for long waves ($ka \ll 1$). However, we shall use a dispersion relation that is shown to be valid for a broader range of wavenumbers, the form of which will be discussed shortly.

A key contribution of Bristol *et al.* (2004) is to recognize that one needs an additional term (given as the fourth column of terms on the right-hand side of (5.5)), which accounts for the orbital rotation of the unequal-strength vortex pair, equivalent to analysing the flow in a reference frame rotating with the vortices. For instability, we require that the perturbation be stationary in the *rotating reference frame* of the pair, so that the perturbation lies close to or along the maximum stretching axis induced by the neighbouring vortex. Bristol *et al.* (2004) demonstrated that this additional term can have a significant effect on the resulting characteristics of the instability.

It still remains to calculate the self-induced rotation rate of the perturbation. Following the analysis of Bristol *et al.* (2004), we begin by considering the equation for the self-induced rotation rate (Γ_i) of a Rankine vortex as presented by Saffman (1992):

$$\sigma_i = \frac{\Gamma_i}{2\pi a_{R,i}^2}\left(\frac{2k}{\sqrt{\kappa_n^2 + k^2}} - 1\right) \quad \text{for } m = 1, \tag{5.8}$$

where κ_n is the the nth root of the dispersion relation for a Rankine vortex (finite core of uniform vorticity with radius a_R), also presented by Saffman (1992). The quantity 'm' represents the azimuthal wavenumber, and takes only integer values. Moore & Saffman (1975) demonstrated that global resonance is possible if two simultaneous perturbations in an external strain field have azimuthal wavenumbers m_a and m_b that satisfy the relation $|m_a - m_b| = 2$. The instabilities predicted by Crow (1970) and Widnall *et al.* (1974) correspond to the resonant interaction of two helical waves with $m = \pm 1$. It is mentioned by Jacquin *et al.* (2003) that this instability mechanism is only possible in the Lamb–Oseen vortex for the case where $m = \pm 1$, and thus we restrict our attention to this case. Owing to symmetry, $\sigma_i(m = +1) = -\sigma_i(m = -1)$, and we can consider only the $m = 1$ wave without loss of generality. The quantity 'n' takes discrete non-negative integer values ($n = 0, 1, 2, \ldots$) and refers to the radial wavenumber or, equivalently, the number of radial nodes.

The first radial mode of instability ($n = 0$) was predicted by Crow (1970) where the vortex core is essentially displaced without internal deformations (see for example figure 2*a*). For this reason, we shall refer to this as the 'displacement mode'. The second radial mode ($n = 1$) corresponds to the short-wave mode predicted by Widnall *et al.* (1974), analysed by Moore & Saffman (1975), and later observed in experiment by Leweke & Williamson (1998) (see for example figure 2*b*). As previously described, this mode is closely related to the elliptic instability and will be referred to as such.

It is additionally important to note that this model only accounts for the externally imposed strain due to the presence of the other vortex, when in reality the strain at the centre of the vortex will be a result of both this externally imposed strain as well as internal strain related to deformation of the vortex core (Robinson & Saffman 1984). This difference will primarily affect the ellipticity of the streamlines and the growth rate of the instability, as discussed in Leweke & Williamson (1998).

In order to apply the analysis to our experiments, we wish to consider the instability of a more realistic distributed vortex rather than simply the Rankine vortex. It was shown by Widnall *et al.* (1971) that the self-induced rotation rates for long displacement perturbations ($ka \ll 1$) were equivalent for both the Rankine (with core radius a_R) and the Lamb–Oseen vortices (with core radius a) provided that

$$a = 0.735 a_R. \tag{5.9}$$

However, Bristol *et al.* (2004) demonstrated by numerical simulation that this equivalence holds reasonably well even for displacement waves with ka_R of the order of unity. In addition, we wish to calculate the self-induced rotation rates of the higher radial modes, although the equivalence given in (5.9) is only shown to apply to the displacement mode. In this paper, we obtain good estimates for the self-induced rotation rates of the higher radial modes ($n \geqslant 1$) for the Lamb–Oseen vortex by employing some results from Le Dizés & Laporte (2002). They present a linear relation that serves as an approximation of the actual dispersion relation, which we interpret for use in our problem:

$$\sigma_i = \frac{\Gamma_i}{2\pi a_i^2}\left[\frac{ka_i - (0.57 + 1.69n)}{2.9 + 4.5n}\right] \quad \text{for } n \geqslant 1,\ m = 1 \tag{5.10}$$

which is a good estimate for the range of wavenumbers that satisfy

$$0.22 + 1.15n < ka_i < 0.92 + 2.23n. \tag{5.11}$$

By inspection of the exact dispersion curves, also presented by Le Dizés & Laporte (2002), it is evident that, for wavenumbers below the range given in (5.11), the linear fit no longer serves as a reasonable approximation. For wavenumbers above the range prescribed in (5.11), the approximation begins to diverge gradually from the exact curve. The actual self-induced rotation rate continues to increase monotonically, suggesting that the linear fit can still be useful to predict qualitative trends. Equipped with the appropriate dispersion relations for the self-induced rotation velocities of perturbations on the core of a Gaussian vortex, we solve to find the growth rate for each selected wavenumber, obtaining the real part of each eigenvalue α.

In order to evaluate the performance of this stability analysis, we compare the results with existing data from numerical simulation performed by So *et al.* (2011), who considered the three-dimensional instability of an isolated unequal-strength counter-rotating Lamb–Oseen vortex pair in an unbounded geometry. The value of Λ was varied from -1 to -0.1, with the core sizes both fixed at $a/d = 0.25$ throughout all simulations. The most unstable wavenumber for each detectable Kelvin mode was reported. We compare our linear stability analysis with the simulations of So *et al.* (2011) in figure 16, yielding reasonable agreement. The results from the simplified linear model compare favourably with the numerical simulation, despite the relatively large core size of the vortices considered. As projected, the use of the approximate dispersion relation for the higher radial modes manages to capture the overall trends of the data nicely.

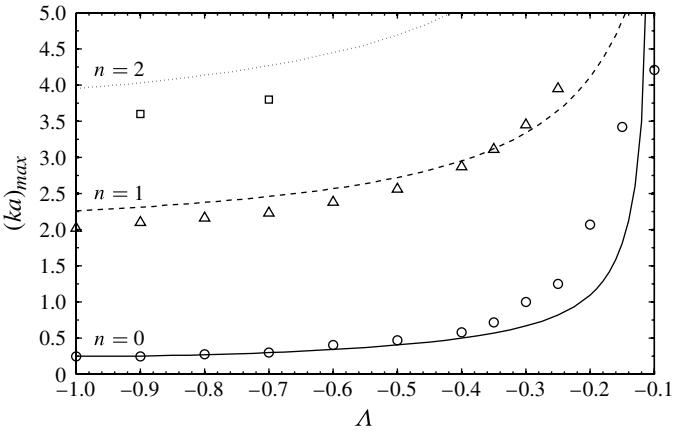

FIGURE 16. The most unstable wavenumber $(ka)_{max}$ versus the strength ratio Λ of an unequal-strength counter-rotating pair, as predicted by the present linear stability analysis (lines) and the numerical simulations of So *et al.* (2011) (symbols). The modes represented are the displacement mode (—, ○), the elliptic instability (− −, △) and the third radial mode (· · · · · ·, □).

An important trend found from the stability analysis, and reflected also in the simulations, is the fact that the most unstable wavelength decreases as the secondary vortex becomes weaker compared to the primary vortex. Another significant point to make is that a measurement of experimental wavelength alone is not sufficient to predict which instability mode is dominant. For example, the simulation demonstrates that the most unstable wavenumber for the $\Lambda = -0.2$, $n = 0$ mode is $ka_i = 2.0$, which is approximately the same wavenumber found for the $n = 1$ mode for vortices of equal strength.

In essence, it seems clear that incorrect conclusions could conceivably be reached if one compares only wavelength measurements to a theory that does not account for the effects of orbital rotation.

5.2. *Analysis of the origin of secondary vortex instability*

In order to apply the linear stability analysis presented in § 5.1 to the present flow, we recognize that a number of assumptions must be made. We assume that the theory holds for vortices of finite core size, which may be highly distorted in the presence of a stronger vortex. We assume that the instability of the secondary vortex is primarily dominated by the adjacent primary vortex, and that the effects of the additional vortex pair across the plane of symmetry are negligible. The strain rate imposed by the presence of the additional pair will scale approximately as $(d/b)^2$, where b is the spacing between the two primary vortices. Note that this ratio is not constant in our experiment, as the proximity of the wall causes the vortex centroids to move apart over time. We estimate that $d/b \approx 1/4$ at the onset of instability, which suggests that the importance of the mirror pair is only minor.

We now apply the linear stability analysis to investigate the origin of our observed short-wave instability of the secondary vortices. Using the experimental measurements from the PIV data for the core size and strengths of the vortices, we use the theory to

predict the most unstable wavenumber of the first two instability modes:

$$(kd)_{max} = 3.53 \quad \text{(displacement mode, theoretical)}, \tag{5.12a}$$

$$(kd)_{max} = 11.7 \quad \text{(elliptic instability, theoretical)}. \tag{5.12b}$$

We can compare this with the experimentally measured instability wavenumber:

$$(kd)_{exp} = 4.8 \pm 1.1 \quad \text{(experimental)}. \tag{5.13}$$

The experimental measurements are presented visually in figure 17, compared with curves representing the most unstable wavenumbers for the first two radial modes, as predicted by the linear stability analysis of § 5.1. Figure 17(*a*) shows the variation of the most unstable wavenumber versus the vortex strength ratio, while figure 17(*b*) demonstrates the influence of core size on the predictions. In essence, the stability theory provides evidence that the origin of the instability is the displacement ($n = 0$) mode, rather than an elliptic instability, as suggested in previous studies.

As a point of interest, we note that, in figure 17(*b*), the wavenumber (kd) of the elliptic instability is shown to decrease for vortices of increasing core size for the range shown. However, if the elliptic instability wavenumber is considered with the more appropriate scaling (as ka rather than kd), the instability wavenumber (ka) increases with increasing core size.

It is clear from the shape of the curves in figure 17 that, even if we allow for considerable error in the measurement of strength ratio or core size, we remain with the conclusion that the instability is dominated by the displacement mode.

This is consistent with our observations in flow visualization, as presented in § 4, where the deformation of the secondary vortices is clearly of the displacement type, illustrating bending of the complete vortex, without evidence of complex internal deformations indicative of elliptic instability.

The range of observed wavelengths observed in experiment, as evident in figure 14, is represented by the vertical bars extending from the experimental data point in figure 17. The observation of a range of wavelengths is consistent with the theory, which suggests that, as the vortex strength ratio is decreased, the band of unstable wavenumbers is widened.

Finally, we observe that the wavelength of the secondary vortex instability is clearly selected before there is any apparent deformation of the primary vortex. This is particularly clear in figure 18, where the secondary vortex is shown to have already undergone significant deformation, yet the primary vortex remains almost perfectly straight. This observation confirms our assertion in § 2 that instabilities do not develop on the primary vortex pair prior to its interaction with the secondary vortex.

5.3. *Discussion of related studies of secondary vortex instability*

In table 1, we compile data coming from previous studies of secondary vortex instability, all of which comprise numerical simulations. There seem to be two common approaches to the three-dimensional problem. The first method, taken by Luton & Ragab (1997) as well as Duponcheel *et al.* (2009), is direct numerical simulation (DNS), where the Navier–Stokes equations are solved numerically. As Reynolds number is increased, the smallest relevant lengths scales in the problem are further reduced, requiring an increase in resolution, which can quickly become prohibitively costly. Both Luton & Ragab (1997) and Duponcheel *et al.* (2009) demonstrate that their respective simulations are properly resolved, at the Reynolds numbers they select, at least with respect to the characteristics of secondary vortex instability. Moet (2003) and Georges *et al.* (2006) use a large-eddy simulation (LES),

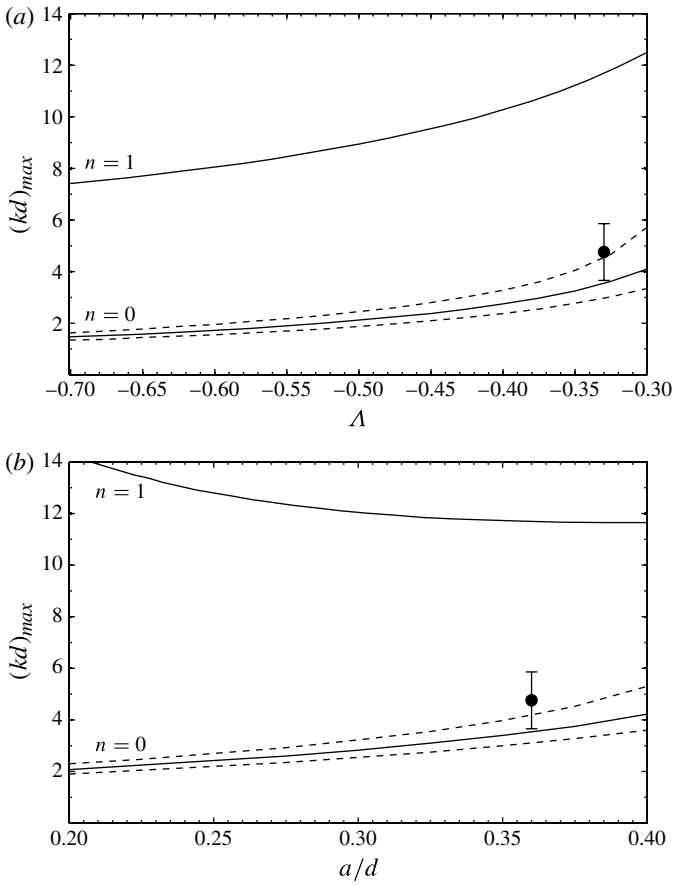

FIGURE 17. Variation of most unstable wavenumber $(kd)_{max}$ versus (*a*) vortex strength ratio and (*b*) core size, using experimentally measured parameters. The solid lines represent the first two radial modes ($n = 0, 1$), as predicted by the linear stability analysis. The filled circle represents the mean wavenumber measured in our experiments, and the vertical bars extend one standard deviation above and below the mean value. The dashed lines represent the most unstable wavenumbers for the displacement mode ($n = 0$) predicted by using (*a*) core size $\pm 15\,\%$ and (*b*) strength ratio $\pm 10\,\%$ different from the experimentally measured value.

whereby the smallest length scales are modelled using a subgrid-scale (SGS) model, reducing the range of length scales that must be resolved and allowing for higher-Reynolds-number cases to be investigated more practically. To account for the smaller-scale vorticity generated at the wall, Georges *et al.* (2006) employ a 'wall-resolved' LES method, which resolves the finer scales of the flow in the proximity of the wall. High resolution at the wall was demonstrated to be essential in the two-dimensional simulations of Clercx & Bruneau (2006) and Kramer *et al.* (2007). Fewer published works are available as compared to the two-dimensional case, possibly due to the greatly increased computational demand.

Both Luton & Ragab (1997) and Duponcheel *et al.* (2009), as well as Moet (2003) and Georges *et al.* (2006), attribute their secondary vortex instability to elliptic instability or radial modes ($n = 1$). In the latter three studies, it is shown that the incipient axial vorticity perturbation structure has the distribution indicative of an

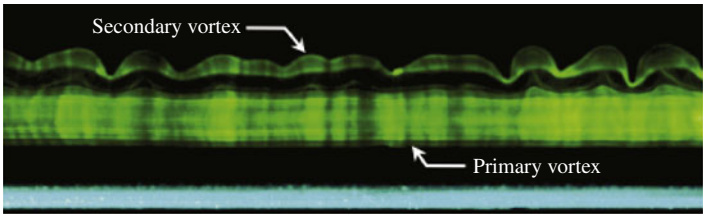

FIGURE 18. Incipient instability of secondary vortex as it passes over the top of the primary vortex. Only one of the primary vortices is marked here. The secondary vortex has already undergone significant deformation while the primary vortex remains almost completely straight.

		Re	Resolution	r_{c1}/b_o	r_{c2}/b_o	λ/b_o	λ/r_{c2}
Present results	Exp.	1260	—	0.39	0.30	0.98	3.27
Luton & Ragab (1997)	DNS	2196	$64 \times 64 \times 128$	0.25	—	0.80	—
Duponcheel *et al.* (2009)	DNS	3500	$512 \times 320 \times 256$	0.22	0.25	0.57	2.29
Duponcheel *et al.* (2009)	DNS	5200	$512 \times 320 \times 256$	0.19	0.23	0.40	1.74
Georges *et al.* (2006)	LES	20 000	$512 \times 256 \times 256$	0.05	—	0.29	—
Moet (2003)	LES	294 000	$111 \times 139 \times 32$	0.10	—	0.25	—

TABLE 1. Comparison of studies investigating the instability of the secondary vortex generated by a counter-rotating vortex pair in ground effect. The most unstable wavelength identified in each study is given by λ. As indicated in the second column, the results are either from experiment (Exp.), direct numerical simulation (DNS), or large-eddy simulation (LES).

elliptic instability (see e.g. Waleffe 1990). In some locations, the structure of the instability brings the outer layers of the secondary vortex closer to the primary, which then become wrapped around the primary vortex. In the case of Luton & Ragab (1997) and Duponcheel *et al.* (2009), the initial conditions of the vortex pair simulations are similar to those of the present study, and we shall primarily focus on these two studies in this section.

Luton & Ragab (1997) find a most preferred wavelength of $3.20r_c$, which they state 'agrees extremely well with the analysis of Widnall *et al.* (1974) which predicts $3.22r_c$, for the second radial mode'. This would appear to provide evidence that the secondary vortex is subject to an elliptic instability. They also detect a further instability of shorter wavelength, which they propose is a representation of the third radial mode ($n = 2$). However, in scaling their secondary instability wavelength, they use the core radius of the larger primary vortex, rather than the radius of the smaller secondary vortex itself. The secondary vortex is the one that exhibits a large-amplitude instability in the presence of a stronger (almost straight) primary vortex. Additionally, their analysis does not take into account the angular rotation of the two unequal vortices, which would significantly affect the prediction of most unstable wavelength, as we have shown in the previous sections.

If we similarly chose to scale our experimental instability wavelength of the secondary vortex with the core size of the primary vortex, we find $ka_1 = 2.24$. The value predicted by Eloy & Le Dizés (1999) for the most unstable wavenumber for

the elliptic instability of the equal-strength counter-rotating Lamb–Oseen vortex pair is $ka = 2.26$, which compares very well. We would conclude, as did Luton & Ragab (1997), that our secondary vortex exhibited an elliptic instability (second radial mode, $n = 1$).

However, the above deduction would be erroneous. In fact, we find that the stability theory presented in the previous sections predicts a theoretical elliptic instability wavelength of $ka_2 = 4.21$, when based on the secondary vortex radius, and including the effects of unequal vortices on the analysis. This more complete analysis points to the origin of the instability, in our work, as the Crow-type displacement mode.

In the work of Duponcheel *et al.* (2009), the elliptic instability observed via the vorticity perturbations is shown to correspond to the highest peak in the axial energy spectra, which is $\lambda/b_o = 0.4$ for the simulation at $Re = 5200$. However, they also mention that a further peak is present with a longer wavelength corresponding to $\lambda/b_o = 1.0$, yet the origin of this peak is not discussed.

The wavelengths of the instability observed in the present experiments are $\lambda/b_o = 1.0 \pm 0.1$, which is comparable to the most unstable wavelength observed in the simulation of Luton & Ragab (1997) ($\lambda/b_o = 0.8$), and to the second peak in the spectra of Duponcheel *et al.* (2009), mentioned above. It seems conceivable that both of these previous studies exhibit the Crow-type displacement mode. In fact, the images showing the deformations of the secondary vortex in the Luton & Ragab (1997) study appear to represent primarily the bending of the secondary vortex as a whole. The fact that an elliptic instability, of shorter wavelength, initially makes itself felt in the research of Duponcheel *et al.* (2009) could perhaps be related to the higher Reynolds numbers of that study, enabling the elliptic instability to manifest itself early in the development of the flow.

6. Dynamics and merging of vortex rows

In this section, we shall analyse and further illustrate the tendency of the deformed secondary vortices on each side of the flow to translate towards each other and to merge into a single row of vortical structures in the centre of the flow field, between the two primary vortices. We shall briefly analyse the dynamics of periodic rows of point vortices. We will see that there are essentially three different types of vortex dynamics possible. Two of these types lead to the vortex rows from each side of the flow translating towards each other, and to possible vortex merging, and thereby to the interesting phenomenon whereby two rows of vortices combine to form a single row.

As the secondary vortex becomes highly distorted due to the bending instability in the presence of the primary vortex, as shown clearly in the side view sequence of figure 15, the highly stretched vertical vortex tubes appear to pair up and translate towards the centre of the flow configuration. If we visualize the evolution of the secondary vortices by using a thin horizontal light sheet parallel to the ground plane (as shown in figure 12*b*), and viewing the flow vertically as indicated by the white arrow, we can most clearly observe these interesting dynamics. In these studies, the plate edge has the very small perturbation (of amplitude 0.5 mm) mentioned in § 2.

The vortex evolution is clearly shown in this light sheet in figure 19. We have chosen to mark only the secondary vorticity with dye, which is key to clear visualization of the phenomena. We observe two ‘infinite’ rows of miniature counter-rotating vortex pairs in the plane of the light sheet, which are advected into the region between the primary vortices. The two rows approach each other and begin to interact in figure 19(*b*). From here we typically observe in figure 19(*c*) that the two rows

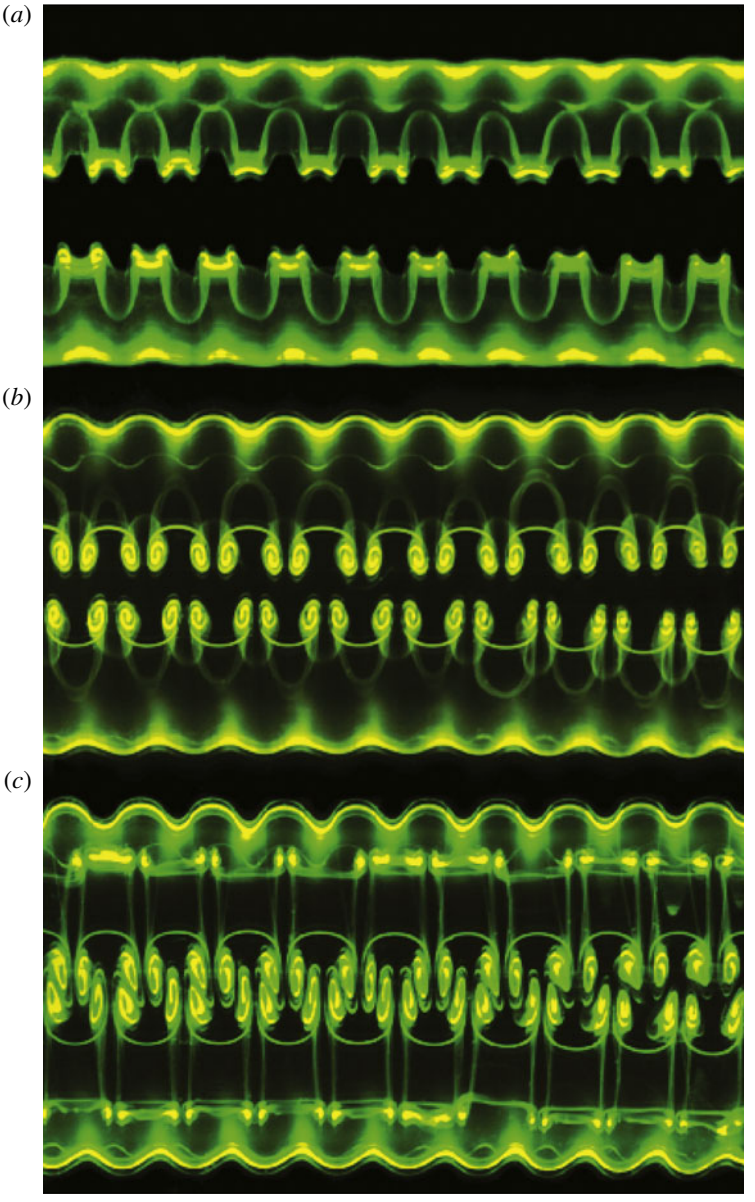

FIGURE 19. Evolution of secondary vortices in the cross-sectional view described by figure 12(*b*). (*a*) The deformed secondary vortices begin to descend through the light sheet. (*b*) The emergence of two 'infinite' rows of vortex pairs (vertical segments) is now apparent. (*c*) The rows move in towards each other, and ultimately merge into a single row. In these experiments, we have introduced a very small-amplitude (0.5 mm) sinusoidal perturbation at the flap tips.

merge into a single row of alternating-sign vortices. This is clearly demonstrated by way of PIV measurements presented in figure 20. We believe that this is the first experimental evidence of the merging of two rows of alternating-sign vortices into a single row.

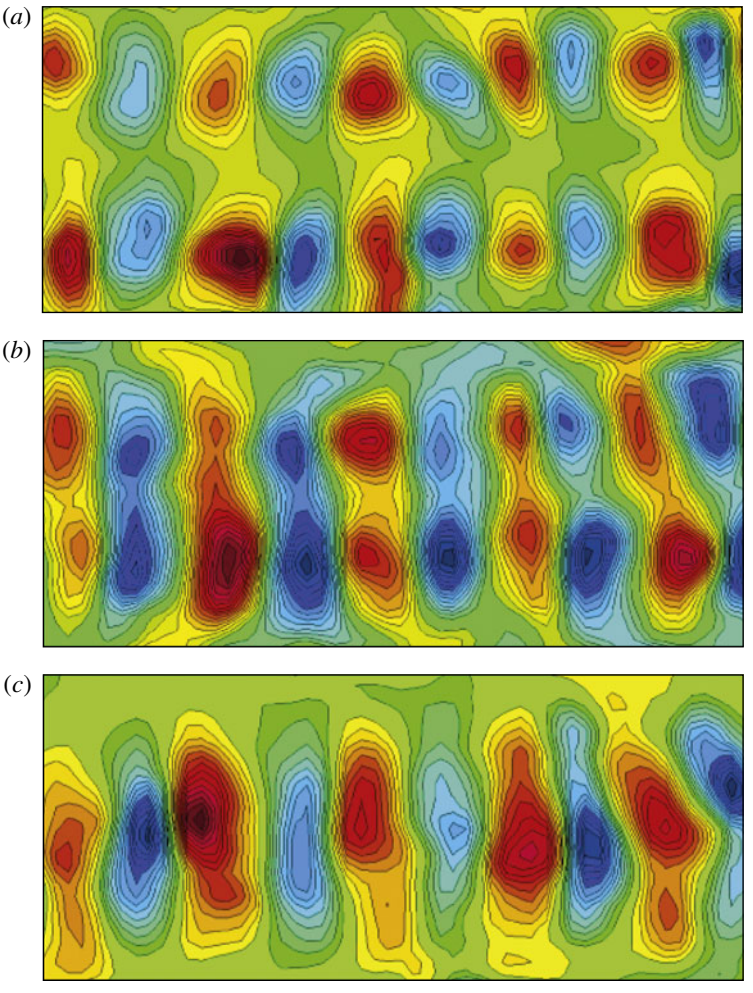

FIGURE 20. Contours of vorticity as calculated using PIV data from a single experiment, measured in a horizontal plane (as shown, for example, in figure 12*b*) at a height of $y \approx 1.5b_o$, with a window of approximately $5b_o \times 2b_o$. (*a*) Two periodic rows of counter-rotating vortices emerge between the primary vortices. (*b*) The rows move in towards each other and begin to merge. (*c*) The merging process is completed, and a single periodic row of counter-rotating vortices results. The vorticity contours levels are redefined at each time step; the measurements are only intended to demonstrate the qualitative evolution of vorticity. In these experiments, we have introduced a very small-amplitude (0.5 mm) sinusoidal perturbation at the flap tips.

As a further illustration of this phenomenon, we shall now consider a two-dimensional point vortex model to represent the dynamics of the vertical vortex segments cutting through the light sheet. The flow field and relevant parameters are defined in figure 21, where the flow is infinitely periodic in L (the wavelength of the secondary vortex instability). A similar analysis showing vortex trajectories for such a four-vortex row system described below has been presented in Williamson (1982) and in Stremler *et al.* (2011), where the motivation was to represent the dynamics

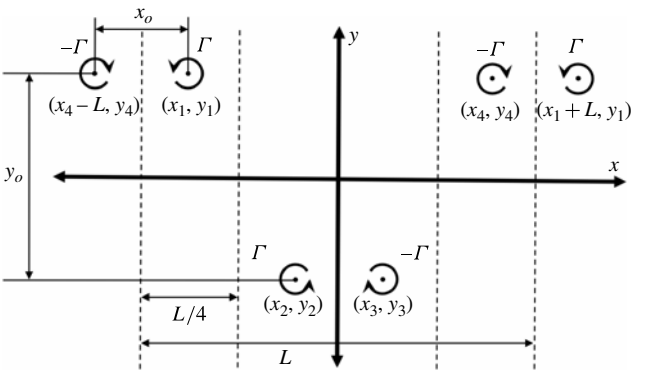

FIGURE 21. Schematic diagram defining the parameters of the point vortex model. The entire flow is periodic in L, which in the present application is equivalent to the wavelength of the instability.

of vortices in the wake of a bluff body or an oscillating aerofoil. The reader is also referred to extensive works on this kind of approach to understanding vortex dynamics, using point vortex analysis, as carried out by Hassan Aref and his group (see e.g. Aref & Stremler 1996, 1999).

To simplify the problem, we assume the vortices to be all of equal strength Γ, and we consider a number of spatial symmetries:

$$\begin{aligned} x_1 &= -x_2 - \tfrac{1}{2}L, \quad & y_1 &= -y_2, \\ x_3 &= -x_2, & y_3 &= y_2, \\ x_4 &= x_2 + \tfrac{1}{2}L, & y_4 &= -y_2. \end{aligned} \tag{6.1}$$

This represents the fact that we have assumed that each miniature vortex pair is equally spaced from one another, and identical otherwise. We can now describe the initial flow field using only two parameters, the initial pair spacing $0 < x_o < L$, and the initial row separation $0 \leqslant y_o < \infty$ (see figure 21). Note that $x_o \in \{0, L\}$ are degenerate cases where vortices of opposite sign coincide, and are ignored here. The equation for the velocity induced by a periodic row of point vortices of strength Γ that are aligned along the x axis with spacing L is given by

$$u(x, y) = \frac{-\Gamma}{2L} \frac{\sinh(2\pi y/L)}{\cosh(2\pi y/L) - \cos(2\pi x/L)}, \tag{6.2a}$$

$$v(x, y) = \frac{\Gamma}{2L} \frac{\sin(2\pi x/L)}{\cosh(2\pi y/L) - \cos(2\pi x/L)}, \tag{6.2b}$$

where u is the velocity in the x direction and v is the velocity in the y direction (see Saffman 1992). We normalize these equations by the length scale $L/(4\pi)$ and time scale $L^2/(2\pi\Gamma)$, yielding

$$U(X, Y) = \frac{-\sinh(Y/2)}{\cosh(Y/2) - \cos(X/2)}, \tag{6.3a}$$

$$V(X, Y) = \frac{\sin(X/2)}{\cosh(Y/2) - \cos(X/2)}, \tag{6.3b}$$

where X and Y are now non-dimensional positions, and U and V are the corresponding non-dimensional velocities. The point vortices will move with the induced velocity field created by all the other vortices in the flow. Our flow of interest can be represented by four infinite rows of like-sign vortices, as indicated in figure 21 by the subscripts 1–4. A single vortex row is stationary, and will move under the induced effects of the other three rows. For example, we can describe the motion of row 2 by the first-order equations

$$\dot{X}_2 = U(X_2 - X_1, Y_2 - Y_1) - U(X_2 - X_3, Y_2 - Y_3) - U(X_2 - X_4, Y_2 - Y_4), \quad (6.4a)$$

$$\dot{Y}_2 = V(X_2 - X_1, Y_2 - Y_1) - V(X_2 - X_3, Y_2 - Y_3) - V(X_2 - X_4, Y_2 - Y_4), \quad (6.4b)$$

where the dot represents the rate of change with respect to the normalized time. Using the symmetry relations provided in (6.1), the motion of row 2 described by equation (6.4) is reduced to a function of only the location of row 2. After simplifying the expression and dropping the subscripts, we find

$$\dot{X} = \frac{-\sinh Y(1 - \cos X)}{(\cosh Y + \cos X)(\cosh Y + 1)}, \quad (6.5a)$$

$$\dot{Y} = \frac{-\sin X(1 + \cosh Y)}{(\cosh Y + \cos X)(1 - \cos X)}. \quad (6.5b)$$

Keeping in mind that $\dot{Y}/\dot{X}$ is equivalent to $\mathrm{d}Y/\mathrm{d}X$, we can then write the slope of a trajectory at any point as

$$\frac{\mathrm{d}Y}{\mathrm{d}X} = \frac{\sin X\ (1 + \cosh Y)^2}{\sinh Y\ (1 - \cos X)^2}. \quad (6.6)$$

This equation is integrable, and thus we can find that a conserved quantity K exists for this flow:

$$K = \frac{\cos X + \cosh Y}{(1 + \cosh Y)(1 - \cos X)}. \quad (6.7)$$

Each value K (which is determined by the initial conditions x_o and y_o) represents a different trajectory in the x–y plane. For fixed (and finite) y_o, we find that three characteristically different types of trajectories are possible by varying x_o between 0 and L.

For small value of x_o, we observe that the rows move in towards each other while also moving closer to their respective partner, as shown in figure 22(a). We describe this as the ‘passing’ mode, as the rows pass through each other, after which the vortex ‘partners’ begin to spread laterally again while the rows continuously move vertically apart.

For intermediate values of x_o, we have the case shown in figure 22(b), where co-rotating pairs, composed of one vortex from each initial row, orbit around one another indefinitely in an ‘orbiting’ mode.

For larger values of x_o, the rows move away from each other at the onset, and continue to do so endlessly in a ‘runaway’ mode, as shown in figure 22(c). Note that the vortices in the passing mode, once the rows have passed each other, will eventually follow the same trajectory as the vortices in the runaway mode, and thus cannot be distinguished solely by the value of K that defines their trajectory.

Figure 22(d) shows a plot of selected vortex (row) trajectories given by (6.7). There are two distinct regions separated by a separatrix (dashed line) in the shape of a

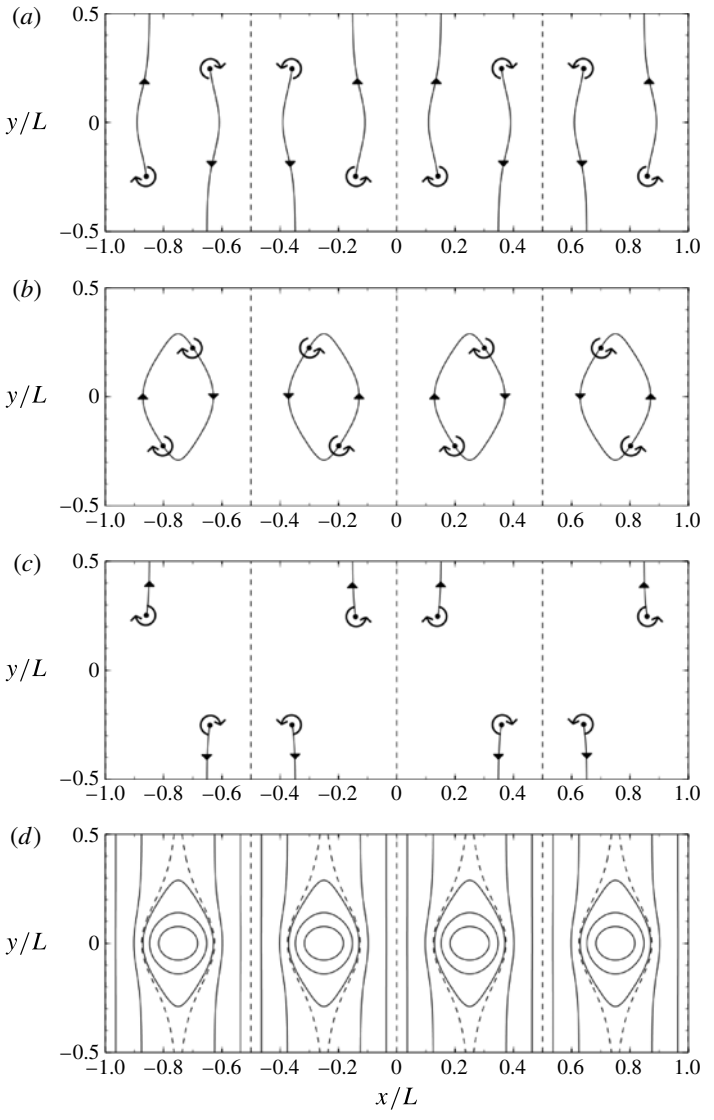

FIGURE 22. Example trajectories for $y_o = 0.5$, as x_o is varied. (*a*) Passing mode, $x_o = 0.3$. (*b*) Orbiting mode, $x_o = 0.4$. (*c*) Runaway mode, $x_o = 0.7$. (*d*) Complete phase plane of solutions. Each curve represents a different value of the conserved quantity K. The separatrices defining the three different regimes are shown as dashed lines.

vertically oriented cat's eye. Trajectories within the separatrix are those representing the orbiting modes, whereas the trajectories outside of the separatrix represent the passing and runaway modes. These different regions can be distinguished by different values of K:

$$\begin{cases} 0 < K < \frac{1}{2} & \text{orbiting mode,} \\ K = \frac{1}{2} & \text{separatrix,} \\ K > \frac{1}{2} & \text{passing or runaway mode.} \end{cases} \tag{6.8}$$

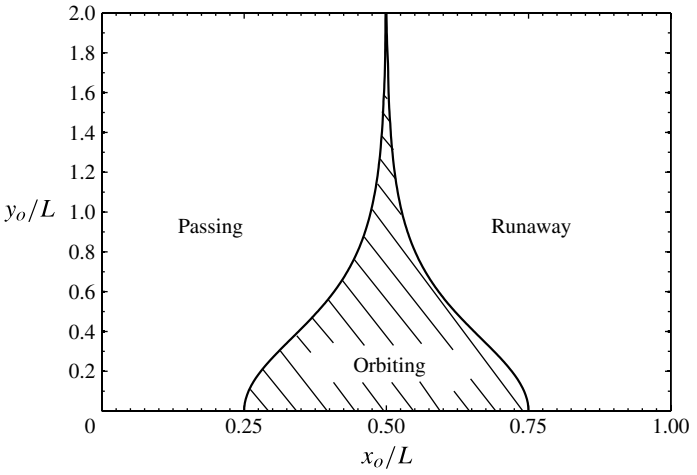

FIGURE 23. Regime diagram for varied initial conditions x_o and y_o. Within each region, one predicts qualitatively similar dynamics. The passing mode is found for small values of x_o/L, the orbiting mode for intermediate values, and the runaway mode for larger values.

Also note that $K = 0$ (for $x_o = L/2$ and $y_o = 0$) represents a degenerate case where vortices of like sign overlap each other, representing a single infinite vortex row of alternating signs, which is a stationary configuration. This is observed in the final stages of the flow, where vortices of like sign have merged at $Y = 0$, as evident in figure 20(*c*). Figure 23 demonstrates that the appearance of a particular mode can be predicted using the two parameters that define the initial conditions of the flow, x_o and y_o.

If one allows for the viscous diffusion of the vortex cores, it is clear that, in the orbiting case, each pair of co-rotating vortices will eventually merge into a single vortex (see Meunier *et al.* 2002; Cerretelli & Williamson 2003). It appears likely that conditions for merger will also occur for some passing mode trajectories. The flow visualizations in figure 19 and the PIV measurements in figure 20 demonstrate such merging of the like-signed vortices. On the other hand, we interpret the passing mode to occur in the images of four-vortex (wing wake) experiments, found in Ortega *et al.* (2003). In the context of vortex–ground interactions, it is possible that different types of secondary vortex trajectories might be observed under different conditions, for example at higher Reynolds numbers. The present vortex dynamics model serves to illustrate possible trajectories of the secondary vortex segments that evolve between the primary vortex structures in this complex flow.

7. Conclusions

In the present work, we study the approach of a descending vortex pair to a horizontal ground plane. We employ a vortex generator submerged in a water tank facility, whereby the closing of flaps hinged to a common base eject fluid vertically downwards, generating a vortex pair.

We briefly present the observed two-dimensional vortex dynamics, and show that the flow underneath an approaching vortex forms a boundary layer on the ground plane. This bounded vorticity can separate to form one or more discrete secondary vortices, of opposite sign to the primary vortex, as found in previous studies. Discrete vortices

are advected around the primary vortex, and induce the primary vortex to apparently 'rebound' from the surface. We explore the effects of *Re* on the characteristics of the secondary vortex generated in ground effect.

As found in previous work, the weaker secondary vortex can become three-dimensionally unstable, in the presence of the stronger primary vortices. It has been suggested in several recent numerical simulations that elliptic instability ($n = 1, 2$) is the origin of such waviness in the secondary vortices (Luton & Ragab 1997; Moet 2003; Georges *et al.* 2006; Duponcheel *et al.* 2009).

In the present research, we employ a technique whereby the primary vortices are visualized separately from the secondary vortices. Fluorescent dye painted onto the flaps is used to mark the primary vortices. However, we also pool dye on the ground plane before an experiment, to mark the secondary vortex separation, often leaving the primary vortices invisible. The use of this simple technique allows us to clearly observe the secondary vortex instability, and indicates that the vortices are bent as a whole in a 'displacement' mode ($n = 0$). The technique, whereby we keep the primary vortices invisible, allows us to see both sides of the flow simultaneously and demonstrates that the instability perturbations on the secondary vortices develop with a distinct antisymmetric phase relationship.

We recognize that another flow, namely the four-vortex wake from a wing with flaps, as studied recently by Crouch (1997), Ortega *et al.* (2003) and Bristol *et al.* (2004), is distinctly similar to our flow field here, although the connection between these flows has not yet been made clear in previous studies. The four-vortex wake comprises a primary wing tip vortex, and a secondary vortex from a wing flap (which can be of opposite sign), on each side of the wake. We analyse the present vortex system by considering a counter-rotating pair, with unequal vortex strength, which is one half of the four-vortex wing wake, as studied by Bristol *et al.* (2004), and note that it is essential to take into account the angular velocity of the weak vortex around the stronger primary vortex in the analysis. We find that the measured secondary vortex wavelength is close to the most unstable wavelength predicted analytically for the displacement bending mode ($n = 0$), similar to the Crow-type instability. The deduction that we have a displacement mode corresponds well with observations, where it is clear that the secondary vortex deforms as a whole. We have analysed the higher-order elliptic instability modes ($n = 1, 2$), by employing the approximate dispersion relation of Le Dizés & Laporte (2002), for the first time in this flow field comprising unequal vortices. We find that the experimental wavelength is distinctly longer than predicted for the higher-order modes.

The fact that the results of Luton & Ragab (1997) suggest a higher mode instability ($n = 1, 2$), when the visualization of their numerical simulations suggests a displacement bending mode ($n = 0$), seems to be related to the fact that they scale the secondary vortex instability on the size of the primary vortex, rather than the secondary vortex itself, and also that their analysis does not take into account the angular rotation effects of the weaker vortex about the stronger one. In fact, in the present work, if we disregard such angular rotation effects in the analysis, we also find results suggesting higher-order instability modes as the origin of our three-dimensional instability. However, this would lead to an incorrect deduction, and illustrates the importance of taking into account angular rotation effects for the unequal vortices.

We must also consider the fact that some numerical studies (Moet 2003; Georges *et al.* 2006; Duponcheel *et al.* 2009) provide evidence for the existence of an elliptic instability mode ($n = 1$), at early times in the simulations, but we note that this appears at higher Reynolds numbers than the present case that was studied in detail.

It was found in Leweke & Williamson (1998) that instabilities could occur together, in the case of an isolated vortex pair; for example, the elliptic instability occurred above a certain critical Reynolds number, simultaneously with the longer-wavelength Crow instability. In the present case, it appears possible that higher-Reynolds-number experiments will exhibit both the elliptic instability as well as subsequently the displacement bending mode instability, which would be consistent with the evidence for the elliptic instability in the numerical simulations.

One of the important aspects of the secondary vortex instability and the development of turbulence in the vortices from aircraft, as discussed by Duponcheel *et al.* (2009), is the resulting decay of the vortices. Such three-dimensional instabilities found here for counter-rotating vortices, lead to turbulence and decay, in a manner similar to many other flows, such as in wakes, jets and shear flows. In the case of the vortex dynamics in a mixing layer (see Brown & Roshko 1974; Konrad 1977; Breidenthal 1981), although in this case the circulation between the two streams remains constant, the three-dimensional instabilities, and the corresponding streamwise vortices, are responsible for the important 'mixing transition' (Bernal & Roshko 1986). In essence, the evolution of turbulent fine-scale structures from three-dimensional instabilities, as observed here in this particular flow, is well known to be generic to shear flows at sufficiently high Reynolds numbers.

Finally, we observe that the secondary vortices deform into a distinct waviness along their lengths, in the presence of the primary vortices, and this places two rows of highly stretched vertical segments of the vortices in between the horizontal primary vortices. The two rows of alternating-sign vortices evolve into miniature vortex pairs, which translate towards each other and ultimately merge into a single vortex row of alternating sign in the centre of the flow field between the primaries. A simple point vortex row model is able to predict trajectories of such vortex rows, which is consistent with the vortex dynamics observed experimentally. The net result of the model's 'orbital' or 'passing' modes is to bring like-sign vortices, from each secondary vortex row, close to each other, such that merging ensues in the experiments.

Acknowledgements

The support from the Ocean Engineering Division of ONR, monitored by Dr T. Swean, is gratefully acknowledged (N00014-07-1-0303). The authors would also like to gratefully acknowledge the New York NASA Space Grant Consortium, run by E. Miles and Y. Terzian, and the Engineering Learning Initiatives, run by Dr L. Schneider at Cornell University, for their student support of this work, while the first author was at Cornell. We additionally wish to extend thanks to V. Miller for his early contributions with the experimental set-up, and to R. Cugnart for enlightening discussions, and for his computational work on the topic.

REFERENCES

AREF, H. & STREMLER, M. 1996 On the motion of three point vortices in a periodic strip. *J. Fluid Mech.* **314**, 1.

AREF, H. & STREMLER, M. 1999 Four-vortex motion with zero total circulation and impulse. *Phys. Fluids* **11**, 3704.

BAYLY, B. J. 1986 Three-dimensional instability of elliptical flow. *Phys. Rev. Lett.* **57**, 2160.

BERNAL, L. P. & ROSHKO, A. 1986 Streamwise vortex structure in plane mixing layers. *J. Fluid Mech.* **170**, 499.

BILLANT, P., BRANCHER, P. & CHOMAZ, J.-M. 1999 Three-dimensional stability of a vortex pair. *Phys. Fluids* **11** (8), 2069.

BREIDENTHAL, R. 1981 Structure in turbulent mixing layers and wakes using a chemical reaction. *J. Fluid Mech.* **109**, 1.

BRISTOL, R. L., ORTEGA, J. M. & SAVAŞ, Ö. 2004 On cooperative instabilities of parallel vortex pairs. *J. Fluid Mech.* **517**, 331.

BROWN, G. L. & ROSHKO, A. 1974 On density effects and large structure in turbulent mixing layers. *J. Fluid Mech.* **64**, 775.

CANTWELL, B. J. 1981 Organized motion in turbulent flow. *Annu. Rev. Fluid Mech.* **13**, 457.

CERRETELLI, C. & WILLIAMSON, C. H. K. 2003 The physical mechanism for vortex merging. *J. Fluid Mech.* **475**, 41.

CLERCX, H. J. H. & BRUNEAU, C.-H. 2006 The normal and oblique collision of a dipole with a no-slip boundary. *Comput. Fluids* **35**, 245.

CROUCH, J. D. 1997 Instability and transient growth for two trailing-vortex pairs. *J. Fluid Mech.* **350**, 311.

CROW, S. C. 1970 Stability theory for a pair of trailing vortices. *AIAA J.* **8**, 2172.

DEE, F. W. & NICHOLAS, O. P. 1968 Flight measurements of wing-tip vortex motion near the ground. CP 1065. British Aeronautical Research Council.

DUPONCHEEL, M., COTTIN, C., DAENINCK, G., WINCKELMANS, G. & LEWEKE, T. 2009 Three-dimensional dynamics of vortex pairs in ground effect: experiment and numerical simulations. *Phys. Fluids* (submitted).

ELOY, C. & LE DIZÉS, S. 1999 Three-dimensional instability of Burgers and Lamb–Oseen vortices in a strain field. *J. Fluid Mech.* **378**, 145.

FABRE, D., JACQUIN, L. & LOOF, A. 2002 Optimal perturbations in a four-vortex aircraft wake in counter-rotating configuration. *J. Fluid Mech.* **451**, 319.

FOGG, J. G. 2001 Vortex pair instabilities in ground effect. Master's thesis, Cornell University.

GEORGES, L., GEUZAINE, P., DUPONCHEEL, M., BRICTEUX, L., LONFILS, T. & WINCKELMANS, G. 2006 LES of two-vortex system in ground effect (longitudinally uniform wakes). Report No. AST4-CT-2005-012238, 6th FAR Wake – Framework Programme for Research and Technological Development, 2005-8.

GERZ, T., HOLZAPFEL, F. & DARRACQ, D. 2002 Commercial aircraft wake vortices. *Prog. Aerosp. Sci.* **38**, 181.

GUPTA, G. 2003 Generation and evolution of a viscous vortex pair. Master's thesis, Cornell University.

HARRIS, D. M., MILLER, V. A. & WILLIAMSON, C. H. K. 2010 A short wave instability caused by the approach of a vortex pair to a ground plane. *Phys. Fluids* **22**, 091106.

HARVEY, J. K. & PERRY, F. J. 1971 Flowfield produced by trailing vortices in the vicinity of the ground. *AIAA J.* **9** (8), 1659.

JACQUIN, L., FABRE, D., SIPP, D., THEOFILIS, V. & VOLLMERS, H. 2003 Instability and unsteadiness of aircraft wake vortices. *Aerosp. Sci. Technol.* **7**, 577.

KELVIN, LORD 1880 On the vibrations of a columnar vortex. *Phil. Mag.* **5** (10), 155.

KONRAD, J. H. 1977 An experimental investigation of mixing in two-dimensional turbulent shear flows with applications to diffusion-limited chemical reactions. PhD thesis, California Institute of Technology.

KRAMER, W., CLERCX, H. J. H. & VAN HEIJST, G. J. F. 2007 Vorticity dynamics of a dipole colliding with a no-slip wall. *Phys. Fluids* **19**, 126603.

LAMB, H. 1932 *Hydrodynamics*, 6th edn. Cambridge University Press.

LE DIZÉS, S. & LAPORTE, F. 2002 Theoretical predictions for the elliptical instability in a two-vortex flow. *J. Fluid Mech.* **471**, 169.

LEWEKE, T. & WILLIAMSON, C. H. K. 1998 Cooperative elliptic instability of a vortex pair. *J. Fluid Mech.* **360**, 85.

LEWEKE, T. & WILLIAMSON, C. H. K. 2011 Experiments on long-wavelength instability and reconnection of a vortex pair. *Phys. Fluids* **23**, 024101.

LIN, J. C. 2002 Review of research on low-profile vortex generators to control boundary-layer separation. *Prog. Aerosp. Sci.* **38**, 389.

LUTON, J. A. & RAGAB, S. A. 1997 Three-dimensional interaction of a vortex pair with a wall. *Phys. Fluids* **9** (10), 2967.

MEUNIER, P., EHRENSTEIN, U., LEWEKE, T. & ROSSI, M. 2002 A merging criterion for two-dimensional co-rotating vortices. *Phys. Fluids* **14**, 2757.

MOET, H. 2003 Simulation numérique du comportement des tourbillons de sillage dans l'atmosphére. PhD thesis, Institut National Polytechnique de Toulouse.

MOORE, D. W. & SAFFMAN, P. G. 1975 The instability of a straight vortex filament in a strain field. *Proc. R. Soc. Lond.* A **346**, 413.

ORLANDI, P. 1990 Vortex dipole rebound from a wall. *Phys. Fluids* A **2**, 1429.

ORTEGA, J. M., BRISTOL, R. L. & SAVAŞ, Ö. 2003 Experimental study of the instability of unequal strength counter-rotating vortex pairs. *J. Fluid Mech.* **474**, 35.

PANTON, R. L. 2001 Overview of the self-sustaining mechanisms of wall turbulence. *Prog. Aerosp. Sci.* **37**, 341.

PEACE, A. J. & RILEY, N. 1983 A viscous vortex pair in ground effect. *J. Fluid Mech.* **129**, 409.

PIERREHUMBERT, R. T. 1986 Universal short-wave instability of two-dimensional eddies in an inviscid fluid. *Phys. Rev. Lett.* **57**, 2157.

ROBINSON, S. K. 1991 Coherent motions in the turbulent boundary layer. *Annu. Rev. Fluid Mech.* **23**, 601.

ROBINSON, A. C. & SAFFMAN, P. G. 1984 Three-dimensional stability of an elliptical vortex in a straining field. *J. Fluid Mech.* **142**, 451.

SAFFMAN, P. G. 1992 *Vortex Dynamics*. Cambridge University Press.

SO, J., RYAN, K. & SHEARD, G. J. 2011 Short-wave instabilities on a vortex pair of unequal strength circulation ratio. *Appl. Math. Model.* **35**, 1581.

SPALART, P. R. 1998 Airplane trailing vortices. *Annu. Rev. Fluid Mech.* **30**, 107.

STREMLER, M. A., SALMANZADEH, A., BASU, S. & WILLIAMSON, C. H. K. 2011 A mathematical model of 2P and 2C vortex wakes. *J. Fluids Struct.* **27**, 774.

TSAI, C.-Y. & WIDNALL, S. E. 1976 The stability of short waves on a straight vortex filament in a weak externally imposed strain field. *J. Fluid Mech.* **73**, 721.

TÜRK, L., COORS, D. & JACOB, D. 1999 Behavior of wake vortices near the ground over a large range of Reynolds numbers. *Aerosp. Sci. Technol.* **3** (2), 71.

VELTE, C. M., HANSEN, M. O. L. & OKLUOV, V. L. 2009 Helical structure of longitudinal vortices embedded in turbulent wall-bounded flows. *J. Fluid Mech.* **619**, 167.

WALEFFE, F. 1990 On the three-dimensional instability of strained vortices. *Phys. Fluids* A **2**, 76.

WIDNALL, S. E., BLISS, D. B. & TSAI, C.-Y. 1974 The instability of short waves on a vortex ring. *J. Fluid Mech.* **66**, 33.

WIDNALL, S. E., BLISS, D. B. & ZALAY, A. 1971 Theoretical and experimental study of the instability of a vortex pair. In *Aircraft Wake Turbulence and its Detection* (ed. J. H. Olsen, A. Goldberg & M. Rogers). p. 305, Plenum.

WILLIAMSON, C. H. K. 1982 Unsteady flows around bluff bodies. PhD thesis, Cambridge University.